Studies of the $t\bar{t}\gamma$ process at $\sqrt{s} = 13$ TeV with the ATLAS detector

Masterarbeit
zur Erlangung des akademischen Grades
Master of Science
(M.Sc.)

vorgelegt von
Stefanie Müller

am 22.04.2025

Eingereicht bei der Naturwissenschaftlich-Technischen Fakultät
der Universität Siegen

2025

Betreuerin und erste Gutachterin:	PD Dr. Carmen Diez Pardos
Zweiter Gutachter:	Prof. Dr. Ivor Fleck

Contents

1 Introduction

THE FORCE
THAT MOVES AND HOLDS THE FORM.

A. S. Byatt

Established in 1954, the CERN (*fr.*: Conseil Européenne pour la Recherche Nucléaire) is one of the greatest scientific projects of its time, uniting people, nations and continents. In this sense, CERN is not only a particle physics laboratory but also a place about cultivating a mindset that fosters respectful collaborations across all boundaries, and creative synergies between science and culture. CERN has become a world laboratory, not only since the discovery of the Higgs boson [1; 9]. Further milestones, all honoured with the Nobel Prize, are the discovery of the W and Z bosons [2–5] and the invention of the multiwire proportional chamber [6]. Over the course of seven decades, the collective intellectual development work at CERN has produced discoveries that have decisively shaped our understanding of the world and are responsible for the success of this unique research institution.

The Large Hadron Collider (LHC), located at CERN, started operating in 2008 and was built to investigate particles at the highest energy scales. This top quark "factory" enables to improve precision of measurements, as well as finding new processes not accessible before. The properties of the top quark, including its coupling to gauge bosons, can be studied in more precise measurements than ever before. The precise knowledge of the couplings of the top quark to the electroweak bosons is of interest as various models beyond the Standard Model that modify these couplings, can be constrained.

The focus of this master's thesis is the study of top quarks in association with photons at the LHC. It contains two studies for proton-proton collisions with a centre-of-mass-energy of $\sqrt{s} = 13$ TeV and a luminosity of $\mathcal{L}$ =140 fb^{-1} collected by the ATLAS detector.

The first part describes the development of a Rivet analysis routine, that allows performing comparisons of experimental data and the theoretical calculations. The routine analyses $t\bar{t}\gamma$ events where either the photon is radiated in the production part or in the total production

and decay stage. The validation of the routine is done with Monte Carlo simulations in the single-lepton and dilepton $t\bar{t}$ decay channels. The Rivet routine is completely validated and available at [7].
The second part comprises the extrapolation of the $t\bar{t}\gamma$ cross section measured at particle level in a fiducial phase space by the ATLAS collaboration in Reference [8] to the full phase space of the $t\bar{t}$ system, to allow for comparisons of the measured results with theory predictions.

This thesis starts by introducing the Standard Model of particle physics and the top quark. The following two chapters concern the ATLAS experiment and the simulations used for the analysis. Chapter 5 introduces to Reference [8] and summarises the results conducted on the same simulations, using different analysis codes. The measured cross sections serve for comparison. The next chapter documents the development of the Rivet routine while chapter 7 is related to the extrapolation of the measured data provided by Reference [8] to the total phase space. Finally, the conclusion is drawn in chapter 8.

2 Theoretical fundamentals of top quark physics

The theoretical foundations for describing top quark physics at hadron colliders is based on the Standard Model (SM) of particle physics, the most precise model to date to represent our physical reality. Describing elementary particles and their interactions, it has become established as an experimental well-tested theory. A large part of the structure given by the SM results from understanding the various symmetries. The following sections provide a brief summary of the SM as well as the fundamental properties of the top quark. Finally, the $t\bar{t}\gamma$ process is examined.

2.1 The Standard Model of Elementary Particle Physics

2.1.1 Overview

The SM of elementary particle physics is the fundamental theory that classifies all known elementary particles and describes three of the four fundamental forces of the universe: the strong nuclear force, the weak nuclear force, and electromagnetism. The force of gravity is not included in the SM, since no common theory of quantum gravity has yet been established.
The mathematical frame of the SM is a gauge theory based on quantum field theory (QFT) which relies on a set of quantum fields as well as their interactions being mediated via the exchange of force carriers. These mediators are particles themselves. Together with the fundamental, indivisible objects of matter they are considered elementary.

Elementary particles are categorized according to their spin. Two types of particles can be defined:

- *Bosons:* Integer spin particles, obeying the Bose-Einstein statistics and comprising the gauge bosons which are the force carriers within the Standard Model, and the so far only known scalar boson, the Higgs boson.

- *Fermions:* Half-integer spin particles, obeying the Fermi-Dirac statistics and sensitive to the interactions carried by the gauge bosons.

Figure 2.1 shows a schematic representation of the SM. The colours indicate the different groups of elementary particles. The fermions with half-integer spin are represented by the quarks and leptons, which are sensitive to a different set of interactions mediated by the force carriers of the interactions, the so-called bosons. The gauge bosons are the force carriers with spin 1. The scalar Higgs boson is the only particle in the SM with spin 0.

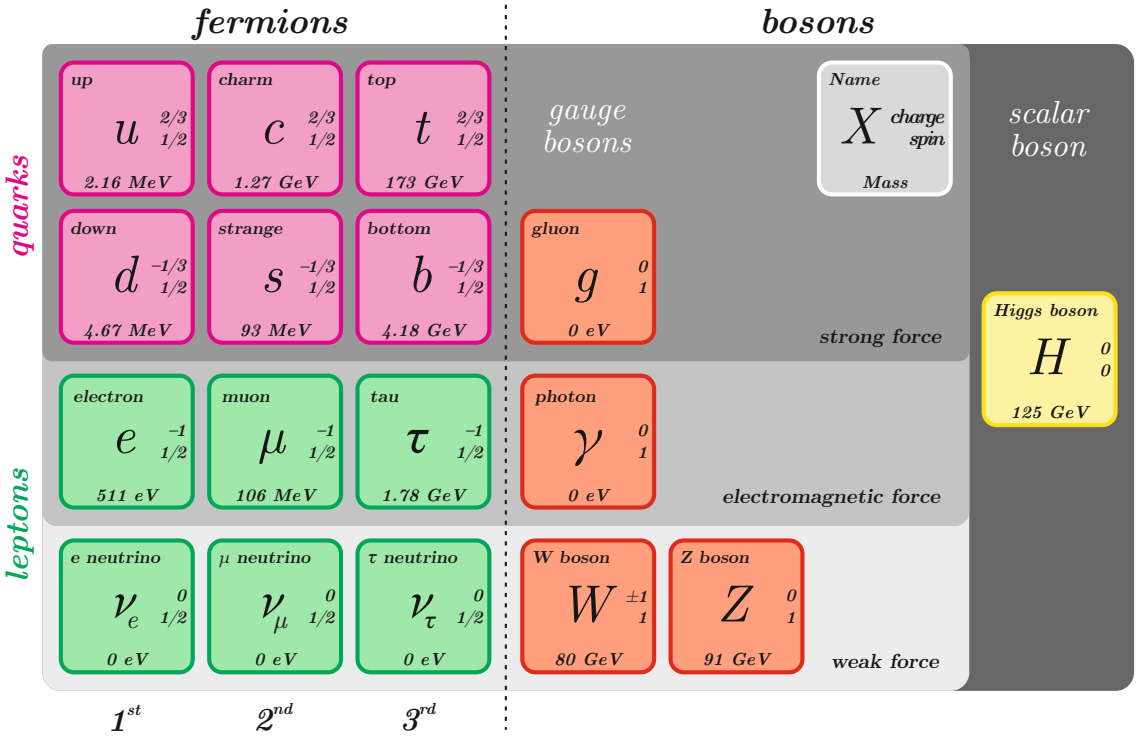

Fig. 2.1: The Standard Model of elementary particle physics.

The elementary particles are explained in more detail below with reference to Figure 2.1. In addition, the antiparticles and the fundamental forces are discussed.

Particles

All known fermions are arranged in three generations. The three different generations of quarks are related in pairs of one up-type-quark with electrical charge of $\frac{2}{3}$ and one down-type-quark with electrical charge of $-\frac{1}{3}$ each, which corresponds to three pairs of quarks: Up and down, charm and strange, top and bottom. Each member of a pair, i.e. each quark-flavour, may be transformed into its partner via the charged-current weak interaction, one of the fundamental forces describing the interactions between particles. Quarks carry colour charge, called red, green or blue. Therefore, there are $6 \times 3 = 12$ quarks

interacting via the strong interaction. According to the nature of the strong interaction, quarks are confined in colourless objects and never appear independently. Instead, they form composite particles called hadrons, which can occur in two different types: A pair of a quark and an anti-quark with a colour-anticolour combination, labelled as meson, and so called (anti-) baryons consisting of three (anti-) quarks each with a different colour.

The six different types of leptons are also known as flavours. They are split up into three particles known as the electron, muon and tau, each with an electric charge of -1. In addition, each lepton is associated with a neutrino, so that the three different generations of leptons are grouped into the three pairs electron and electron neutrino, muon and muon neutrino, and finally tau and tau neutrino. Neutrinos are neutral and predicted to be massless [1] by the SM.

Antiparticles

The SM allows for antiparticles corresponding to each of the fermions. Antiparticles have the same mass and properties to particles but differing in the sign of their additive quantum numbers. Therefore, electric charge and colour charge are reversed.

Fundamental forces and carrier particles

The fundamental forces describing the interactions between the SM particles result from the exchange of force carrier particles, the gauge bosons. Each fundamental force has its own corresponding boson. Table 2.1 shows a graphical overview of the elementary gauge bosons in the SM.

interaction	**relative strength (TeV scale)**	**gauge boson**	**mass of the gauge boson**
strong	1	gluon (g)	~ 1.3 MeV
electromagnetic	$\sim 10^{-2}$	photon (γ)	$< 1 \cdot 10^{-18}$ eV
weak	$\sim 10^{-6}$	boson ($W^{+/-}$)	80.3692 ± 0.0133 GeV
		boson (Z^0)	91.1880 ± 0.0020 GeV

Tab. 2.1: Overview of the interactions described by the SM and the corresponding gauge boson properties [11].

[1] In the SM the neutrino masses are assumed to be zero. However, recent experiments give evidence for neutrinos to be massive, see [10].

The *strong interaction* is represented by the gluon g. Gluons are massless and have no electric charge. By introducing the concept of colours they are responsible for the confinement of quarks in colourless particles, i.e. gluons carry colour charge (r, g, b) that is always made up of a "colour" and an "anti-colour". The possible combinations of colours and anti-colours in gluons result from group theoretical considerations in $SU(3)_C$: $3 \otimes \bar{3} = 8 \oplus 1$. Accordingly, the number of gluons is given by the 8 possible colour charge configurations. The singlet is colourless because it represents a total symmetrical state.

The *electromagnetic interaction* is carried by the photon, which is colourless and has no mass nor electrical charge. It describes the interaction between charged particles, as well as macroscopic charged objects, and it is not limited to any range, although its potential V(r) decreases with the distance r: $V(r) \sim 1/r$.

The *weak interaction* is governed by the exchange of three gauge bosons, the $W^{\pm}$-boson with an electrical charge of ± 1 and the Z^0-boson which is electrically neutral. All gauge bosons are massive and do not have a colour charge. All fermions can interact via the weak interaction which is responsible for radioactive decays, as it is able to change the flavour of quarks by radiating a W boson. Furthermore, it is the only interaction which is able to affect the neutrinos in the SM.

Finally, the masses of the bosons and fermions are obtained by interaction of the particles with the scalar *Higgs field*, represented by the massive scalar Higgs boson which is the only known elementary spin 0 particle.

Together with the six leptons, the twelve quarks constitute all of the known luminous matter in the universe. The understanding of the properties of the quarks and leptons and their interactions are therefore of paramount importance.

2.1.2 Mathematical formulation of the Standard Model

The SM of elementary particle physics is a gauge QFT that relies on a set of fields, describing the fundamental objects, and the gauge symmetries $SU(3)_C \times SU(2)_L \times U(1)_Y$. These internal symmetries [2] of the unitary product group dictate the interactions being mediated via the exchange of force carriers or mediators. $SU(3)_C$ is associated to the strong force and $SU(2)_L$ is related to the weak force. $U(1)_Y$ is not associated with electromagnetism, but to an electromagnetic-like force known as hypercharge. It also affects the weak force. $SU(2)_L$ and $U(1)_Y$ are unified to the electroweak theory $SU(2)_L \times U(1)_Y$. Within QFT the

[2] The subscript merely denotes what property the group acts on: C refers to the colour degree of freedom, L indicates the coupling to only left-handed fermions, the charges are denoted as Y, correspondingly the group of hypercharge is denoted by $U(1)_Y$ to distinguish it from electromagnetism.

electromagnetic interaction described by so called quantum-electrodynamics (QED), the strong interaction via quantum-chromodynamics (QCD). All of the interactions between such fields as well as the motion of particles themselves can be expressed by a Lagrangian density, also referred to as Lagrangian.

For being mathematically self-consistent the Lagrangian of the SM is required to be gauge-invariant, local and renormalizable. It can be divided into several pieces:

$$\mathcal{L}_{\mathrm{SM}} = \mathcal{L}_{\mathrm{Gauge}} + \mathcal{L}_{\mathrm{Fermi}} + \mathcal{L}_{\mathrm{Yukawa}} + \mathcal{L}_{\mathrm{Higgs}}. \tag{2.1}$$

The full expanded form of the Standard Model Lagrangian would exceed the scope of this work. Hereinafter a brief summary of the individual parts is given.

The first two pieces are the kinetic terms for the fields.
The pure gauge Lagrangian is given by

$$\mathcal{L}_{\mathrm{Gauge}} = \frac{1}{2g_S^2} TrG^{\mu\nu}G_{\mu\nu} + \frac{1}{2g^2} TrW^{\mu\nu}W_{\mu\nu} - \frac{1}{4g'^2} TrB^{\mu\nu}B_{\mu\nu}, \tag{2.2}$$

where $\mathrm{G}^{\mu\nu}$, $\mathrm{W}^{\mu\nu}$ and $\mathrm{B}^{\mu\nu}$ are the gluon, weak, and hypercharge field-strength tensors. These terms contain the kinetic energy of the gauge fields and their self-interactions.

The kinetic terms for the fermions are

$$\mathcal{L}_{\mathrm{Fermi}} = i\sum_{i=1}^{3} (\bar{Q}_L^i \not{D} Q_L^i + \bar{u}_R^i \not{D} u_R^i + \bar{d}_R^i \not{D} d_R^i + \bar{L}_L^i \not{D} L_L^i + \bar{e}_R^i \not{D} e_R^i). \tag{2.3}$$

This piece contains the kinetic energy of the fermions and their interactions with the gauge fields, which are contained in the covariant derivatives. The exact form of these kinetic terms depends on the representation of the fermion field. So, for example, Q_L is charged under each of the three gauge fields and has kinetic term

$$\not{D} Q_L = \gamma^\mu (\partial_\mu + i g_S G_\mu + i g W_\mu + i \frac{1}{6} g' B_\mu) Q_L. \tag{2.4}$$

Within these covariant derivatives are the coupling constants: g_S for the SU(3) strong force, g for the SU(2) weak force and g' for the U(1) hypercharge. Their approximate values, evaluated at $\mathrm{M_Z}$, are

$$g_S \approx 1, \qquad g \approx \frac{2}{3}, \qquad g' \approx \frac{2}{3\sqrt{3}}. \tag{2.5}$$

The place where the additional generations add a level of complexity is offered in the Yukawa couplings. In contrast to the gauge couplings, the Yukawa couplings, the next

piece of the Lagrangian, involve the mixing between the different generations. The Yukawa interaction of the Higgs field with the fermions is given by

$$\mathcal{L}_{\text{Yukawa}} = -\Gamma_u^{ij}\bar{Q}_L^i\epsilon\phi^* u_R^j - \Gamma_d^{ij}\bar{Q}_L^i\phi d_R^j - \Gamma_e^{ij}\bar{L}_L^i\phi e_R^j + h.c., \tag{2.6}$$

where $\epsilon = i\sigma_2$ is the total antisymmetric tensor in two dimensions, related to the second Pauli matrix σ_2 and required to ensure each term separately to be electrically neutral. $\Gamma_u, \Gamma_d, \Gamma_e$ replace the coupling constants here with 3×3 matrices and ensure there is a mixing between different generations. These matrices contain most of the parameters of the Standard model.
Finally, the Higgs Lagrangian includes the kinematic energy of the Higgs field, its gauge interactions, and the Higgs potential:

$$\mathcal{L}_{\text{Higgs}} = (D_\mu\phi)^\dagger D^\mu\phi - V(\phi) \tag{2.7}$$

with the SU(2) doublet ϕ containing the complex scalar fields ϕ^+ and ϕ^0

$$\phi = \begin{pmatrix} \phi^+ \\ \phi^0 \end{pmatrix} \tag{2.8}$$

and the potential $V(\phi)$

$$\mathrm{V}(\phi) = \mu^2\phi^2 + \lambda\phi^4. \tag{2.9}$$

The electroweak symmetry breaking mechanism in the SM is described by the two parameters μ and λ which define the shape of the underlying scalar Higgs field potential. Determining the ground state ϕ^0 depends on the sign of μ^2. Choosing $\mu^2 < 0$, with the assumption that $\lambda > 0$, leads to a Higgs field which has a non-zero expectation value v on a circle of minima in the complex plane with radius $\phi^0 = \frac{\mu}{\sqrt{2\lambda}} \equiv \frac{v}{\sqrt{2}}$. Any of these minima breaks the electroweak symmetry and generates masses for the gauge bosons,

$$\mathrm{M_W} = \frac{1}{2}gv, \tag{2.10}$$

$$\mathrm{M_Z} = \frac{1}{2}\sqrt{g^2 + g\prime^2}v. \tag{2.11}$$

In addition, the mass of the Higgs boson can be obtained from the potential term $V(\phi)$ of the Lagrangian:

$$\mathrm{m_H} = \sqrt{2\lambda}v. \tag{2.12}$$

Since the value of the parameter λ is unknown, the mass of the Higgs boson is a free parameter of the SM which has to be determined experimentally. The top quark is of particular interest here, due to its large mass and therefore, its sensitivity to couple to the Higgs boson.

2.2 The top quark

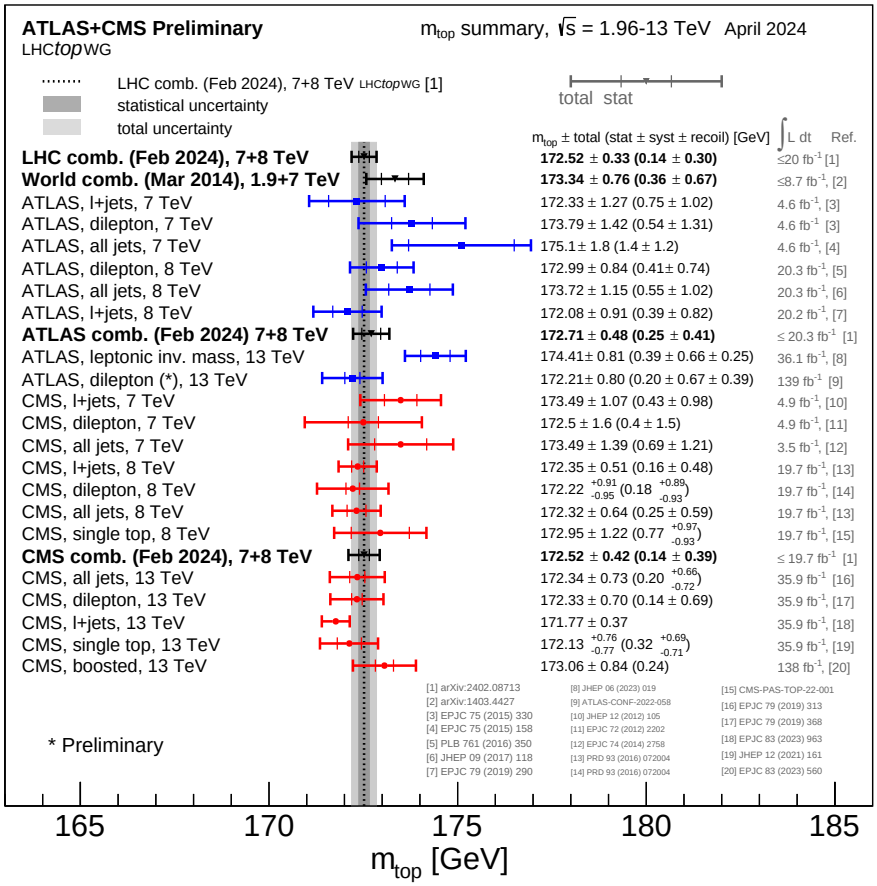

Fig. 2.2: Summary of the ATLAS and CMS direct top mass measurements from top quark decay. The results are compared with the LHC and Tevatron+LHC combinations of the top quark mass m_{Top} [13].

The top quark is the most massive fundamental particle in the SM [14]:

$$m_t = 173.34 \pm 0.76 \text{ GeV}. \tag{2.13}$$

It is part of the third generation of quarks, i.e. the $Q = \frac{2}{3}$, $T_3 = +\frac{1}{2}$ member of the weak isospin doublet containing the bottom quark. Although a third generation was predicted

already in 1973, due to its mass it was only discovered in 1995 at the Tevatron $p\bar{p}$ collider at FNAL. The centre-of-mass energy of 1.8 TeV marked a significant increase compared to earlier experiments, such that the top quark became directly accessible in a collider for the first time. The announcement of the discovery of the top quark took place publicly in a joint seminar of CDF and DØ collaborations at FNAL on March 2, 1995 [15; 16].
Being heavier than all other particles, the top quark has a large decay width and therefore a very short lifetime ($\sim 10^{-25}$ s). This value is so small that top quarks decay before they hadronize which makes the top quark unique among all other quarks. In addition, the top quark is the only quark whose Yukawa coupling to the Higgs boson is in order of unity. For these reasons the top quark plays a special role in the Standard Model and theories beyond. In particular, a detailed knowledge of its properties can provide important information about fundamental interactions at the electroweak breaking scale. Figure 2.2 shows a summary of direct top mass measurements done by ATLAS and CMS at the LHC collider at CERN.

2.2.1 Production

At hadron colliders top quarks are produced dominantly in pairs $t\bar{t}$, mediated by the strong interaction. There are two possible production processes at leading order in QCD:

- gluon-gluon fusion: $gg \to t\bar{t}$
- $q\bar{q}$ annihilation: $q\bar{q} \to t\bar{t}$

Figure 2.3 shows top quark pair production via strong interaction at hadron colliders which happens at lowest order through gluon-gluon fusion and quark-antiquark annihilation.

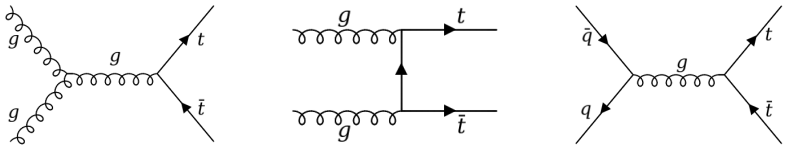

Fig. 2.3: Diagrams of $t\bar{t}$ production at lowest order QCD with gluon-gluon fusion (*left* and *middle*) and quark-antiquark annihilation *(right)*.

At the LHC 80-90% of $t\bar{t}$ pairs are created via gluon-gluon fusion, increasing with the centre-of-mass energy $\sqrt{s}$, what makes the LHC known as a real top quark factory. The predicted $t\bar{t}$ cross section compared to the observed ones as a function of the centre-of-mass energy for pp and $p\bar{p}$ collisions can be seen in Figure 2.4. The predicted cross section is calculated at next-to-next-to-leading order (NNLO) in α_s and complemented with a next-to-next-to-leading-log order (NNLL).

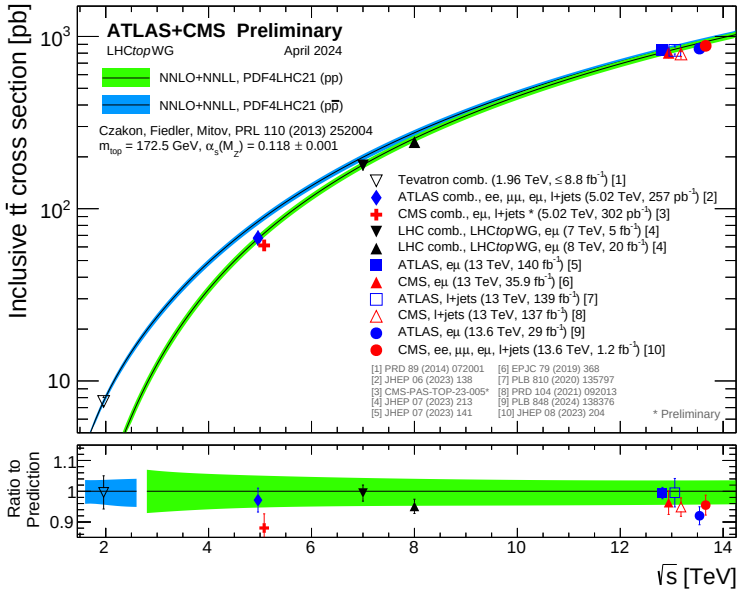

Fig. 2.4: Summary of LHC and Tevatron measurements of the top-pair production cross-section as a function of the centre-of-mass energy compared to the NNLO QCD calculation complemented with NNLL resummation [13].

For completeness it should be mentioned that the Standard Model also predicts electroweak production of single top quarks. Single top quark production was observed for the first time by CDF and DØ in 2009 [17; 18]. In this thesis the focus is on top quark pair production.

2.2.2 Decay

The uniqueness of the top quark is based on the property that it decays before it can hadronize. Its large mass results in a lifetime ($\sim 10^{-25}$ s) that is shorter than the time that is needed for strong interactions to bind into a hadron or to modify its properties, since the time scale of the strong interaction is a magnitude lower ($\sim 10^{-24}$ s).
The top quark decays via the weak interaction to another quark flavour, with a probability given by the Cabibbo-Kobayashi-Maskawa (CKM) matrix:

$$V_{CKM} = \begin{pmatrix} V_{ud} & V_{us} & V_{ub} \\ V_{cd} & V_{cs} & V_{cb} \\ V_{td} & V_{ts} & V_{tb} \end{pmatrix} \tag{2.14}$$

The current values for each matrix element are given in Table 2.2.

matrix element	**experimental value (average)**
$\lvert V_{ud}\rvert$	0.97370 ± 0.00014
$\lvert V_{us}\rvert$	0.2245 ± 0.0008
$\lvert V_{ub}\rvert$	0.00382 ± 0.00024
$\lvert V_{cd}\rvert$	0.221 ± 0.004
$\lvert V_{cs}\rvert$	0.987 ± 0.011
$\lvert V_{cb}\rvert$	0.0410 ± 0.0014
$\lvert V_{td}\rvert$	0.0080 ± 0.0003
$\lvert V_{ts}\rvert$	0.0388 ± 0.0011
$\lvert V_{tb}\rvert$	1.013 ± 0.030

Tab. 2.2: The magnitudes of the independently measured CKM elements [19].

Since the $|V_{tb}|$ element is very close to one the top quark almost exclusively decays to a W boson and bottom quark. Any other possible decays to a strange and charm quark or an up and down quark are highly suppressed.

Allowing for $t \to Wb$ the final states for the leading pair production process of $t\bar{t}$ can be divided into three classes referred to as the (I) all-hadronic, (II) single-lepton (ℓ+jet), and (III) dilepton channels ($\ell\ell$), respectively [20].

I. $t\bar{t} \to W^+bW^-\bar{b} \to q\bar{q}'bq''\bar{q}'''\bar{b}$, (45.7%)

II. $t\bar{t} \to W^+bW^-\bar{b} \to q\bar{q}'b\ell^-\bar{\nu}_\ell\bar{b} + \ell^+\nu_\ell bq''\bar{q}'''\bar{b}$, (43.8%)

III. $t\bar{t} \to W^+bW^-\bar{b} \to \ell^+\nu_\ell b\ell'^-\bar{\nu}_{\ell'}\bar{b}$ (10.5%)

The branching ratios for $t\bar{t}$ given above include $W \to \tau$ as the decay products of the τ are added to the corresponding channels.

Figure 2.5 illustrates the dileptonic decay channel of the $t\bar{t}$ system.

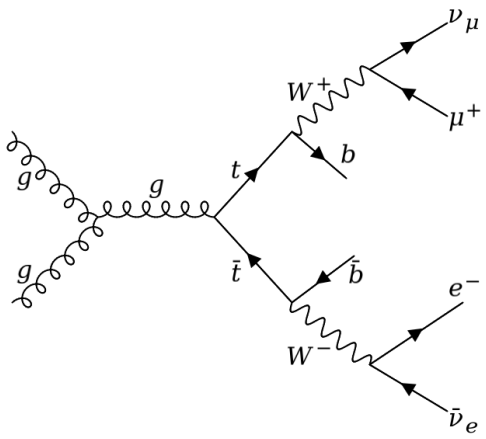

Fig. 2.5: Diagram of the dileptonic decay channel of the $t\bar{t}$ system.

2.3 Top quark pairs in association with a photon

In 2011 the CDF Collaboration reported the first evidence for the production of a top quark pair in association with an energetic, isolated photon [21]. It was found in proton-antiproton ($p\bar{p}$) collisions at the Tevatron collider at a centre-of-mass energy of $\sqrt{s} = 1.96$ TeV. The observation of the $t\bar{t}\gamma$ process was established by the ATLAS Collaboration with the data collected at $\sqrt{s} = 7$ TeV in 2015 [22].

At the LHC top quark pairs are produced in large quantities which provides ideal opportunities to study properties of the top quark such as the associated production of a top quark pair with one of the electroweak bosons W, Z or γ. Figure 2.6 shows a summary of recent ATLAS and CMS measurements of $t\bar{t} + X$ (with X = W, Z or γ) cross section at 13 TeV.

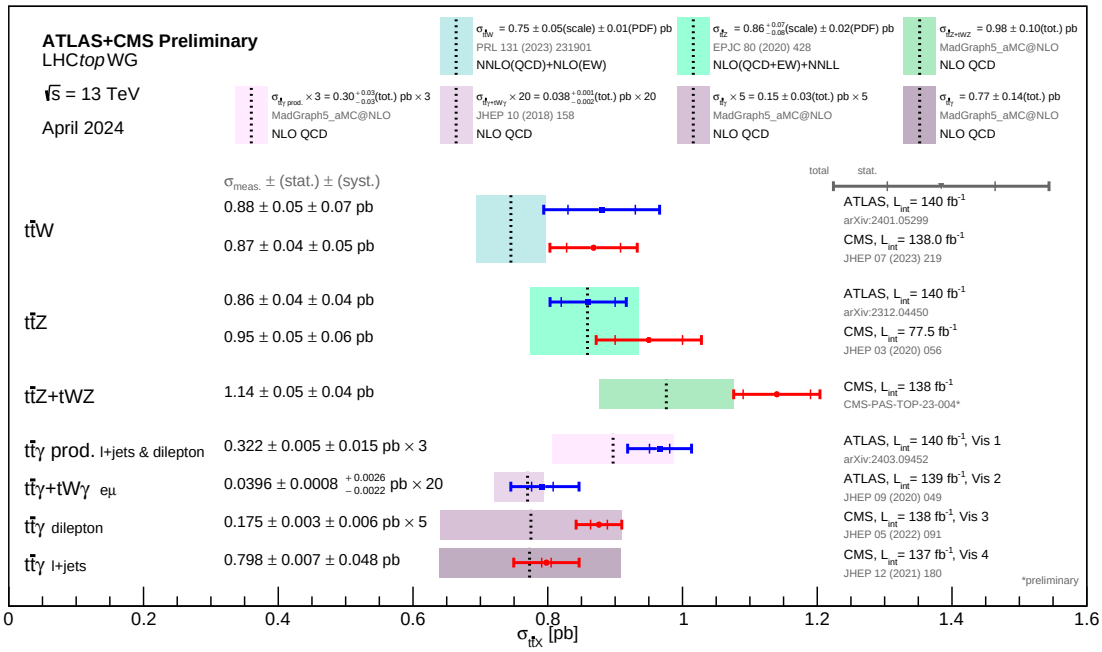

Fig. 2.6: Summary of ATLAS and CMS measurements of $t\bar{t} + X$ (X = W, Z or γ) cross sections at 13 TeV. The $t\bar{t}\gamma$ measurements are compared to NLO QCD theoretical calculations [13].

In this study, the main focus is on the $t\bar{t}\gamma$ process, i.e. top quark pairs in association with a photon, the force carrier of the electromagnetic interaction. As can be seen in Figure 2.6 top quark pair production in association with a photon has a small cross section in proton-proton collisions.

Theoretical studies with the narrow width approximation (NWA) [23] reveal kinematic differences between events of $t\bar{t}\gamma$ where either γ results from production or decay. This enables a separation of all $t\bar{t}\gamma$ samples in one of two kinds:

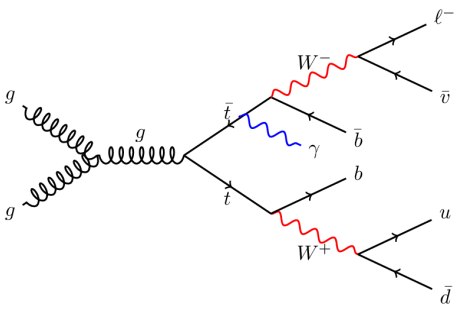

Fig. 2.7: The $t\bar{t}\gamma$ production process.

$t\bar{t}\gamma$ production

Example of leading-order Feynman diagram for $t\bar{t}\gamma$ production in the $t\bar{t}$ single-lepton final state [8]. The photon is radiated by an off-shell top quark [8]. The term $t\bar{t}\gamma$ production refers to the process where the photon is emitted in the top quark production stage. Thereby the photon can be radiated from an initial state parton or from an off-shell top quark [8]. The production of $t\bar{t}\gamma$ is sensitive to the coupling between the top quark t and the photon γ (tγ coupling). This is of interest because constraining the $t\bar{t}\gamma$ coupling allows to probe several BSM models, which modify the coupling.

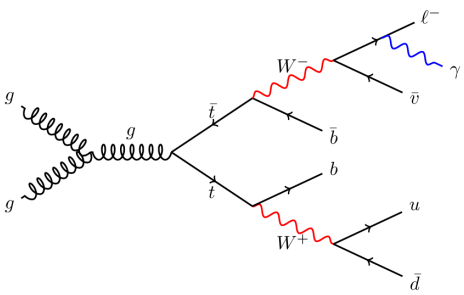

Fig. 2.8: The $t\bar{t}\gamma$ decay process.

$t\bar{t}\gamma$ decay

Example of leading-order Feynman diagram for $t\bar{t}\gamma$ decay in the $t\bar{t}$ single-lepton final state [8]. The photon is radiated by a charged lepton [8]. The term $t\bar{t}\gamma$ decay alludes to the processes, where photons are radiated from on-shell top quarks or any of the charged decay products of the top quark. It is challenging to experimentally separate the $t\bar{t}\gamma$ decay process due to the fact that $t\bar{t}\gamma$ production gives similar kinematic properties.

Theoretical studies with the narrow width approximation (NWA) enable to calculate each process separately and reveal kinematic differences between the events where either γ results from production or decay.

Figure 2.9 shows differential cross section distributions of $t\bar{t}\gamma$ production in comparison to $t\bar{t}\gamma$ decay at 13 TeV as function of the kinematic distribution S_T which is defined as the sum of transverse momentum of leptons, jets and photons:

$$S_T = \sum p_T^{leptons} + \sum p_T^{jets} + \sum p_T^{\gamma} \quad (2.15)$$

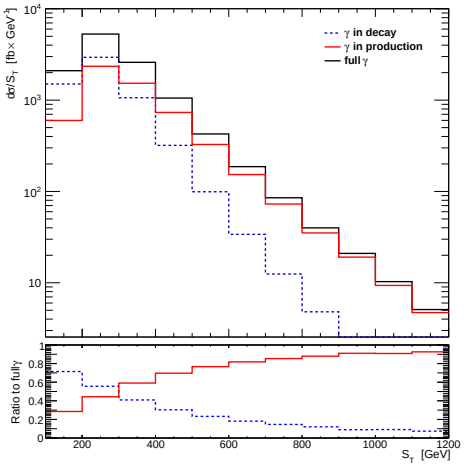

Fig. 2.9: Differential cross section distribution of $t\bar{t}\gamma$ production in comparison to $t\bar{t}\gamma$ decay at 13 TeV as a function of the kinematic distribution S_T (Eq. 2.15).

As can be seen in Figure 2.9 for low values of S_T, the differential distributions are dominated by emission from the decay stage. However, once the high S_T regions are probed, emission from the production part of the $t\bar{t}\gamma$ process dominates completely the full result. This shows that proper modelling of the top quark production and decays is essential even in the presence of inclusive cuts. Based on this result, selection criteria can be developed to reduce such contributions that constitute a background for the measurement of $t\bar{t}\gamma$ properties. In the following studies, the $t\bar{t}\gamma$ production process is considered signal, while $t\bar{t}\gamma$ decay events are background processes.

The MC sample used in this analysis for $t\bar{t}\gamma$ production is calculated at NLO and referred to as the "$t\bar{t}\gamma$ production" sample in the following. The second sample, where the photon arises from any of the decay products of the top quark or from one of the on-shell top quarks, is simulated at LO precision followed by the decay of the top quarks, which is also simulated with LO accuracy. This sample is designated as "$t\bar{t}\gamma$ decay" sample. Both samples were generated with the MadGraph5_aMC@NLO generator by using the NNPDF3.0nlo [24] parton distribution function (PDF) set. A more detailed description of the MC samples can be found in chapter 4.

3 Experimental setup of the ATLAS experiment

ATLAS is a particle physics experiment at LHC built to study the constituents of matter and answer fundamental questions in physics. The laboratory complex is located at the border of France and Switzerland, close to the city of Geneva and with the LHC it provides the largest particle accelerator in the world. In the following the LHC and the ATLAS experiment will be introduced.

3.1 The Large Hadron Collider

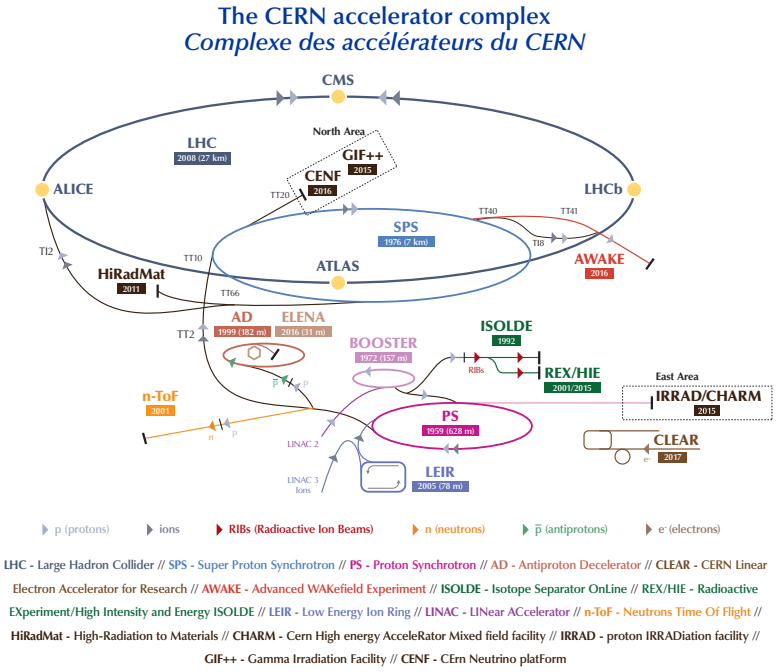

Fig. 3.1: The CERN accelerator complex [25].

The LHC is a circular particle accelerator with a circumference of 26.7 km constructed for colliding protons and ions. Two beams are accelerated in opposite directions along the ring of superconducting magnets with 1232 dipole magnets to keep the beams in the ring, and 392 quadrupole magnets to focus them. The beams collide at the collision points of one of the four experiments, corresponding to the positions of the four particle detectors ATLAS, CMS, ALICE and LHCb. The LHC is a prolific source of top quarks with about 8 million $t\bar{t}$ events per year. Thereby the force carrier of the strong interaction, the gluon is the driving factor in the creation of initial states via gluon-fusion for the proton-proton collisions.

As can be seen in Figure 3.1, there are several steps for acceleration. The protons are obtained from a hydrogen source and are pre-accelerated in the LINAC to energies of 50 MeV. After that they enter the Synchrotron Booster, which increases the energy up to 1.4 GeV. Injection into the Proton Sychotron (PS) and the Super Proton Synchrotron (SPS) leads to successive acceleration of the protons to energies of 25 GeV to 450 GeV, respectively, before they enter the LHC, where they are accelerated to the final centre-of-mass energy of 13.6 TeV and brought to collision. The collisions occur at a rate of 40 MHz for every colliding pair of bunches from the two proton beams. The bunch spacing is 25 ns.
In addition to colliding protons, the LHC is also able to accelerate and collide heavy ions. Apart from using a different LINAC for the first acceleration step, the procedure is the same as described above.

A standard for the performance of the LHC is the delivered integrated luminosity, which is measured by the amount of data taken by the corresponding experiment. The (instantaneous) luminosity $\mathcal{L}$ is related to the observed event rate

$$\frac{\mathrm{dN_{event}}}{\mathrm{dt}} = \mathcal{L} \cdot \sigma_{\mathrm{event}}, \tag{3.1}$$

where σ_{event} is the cross section of the observed process. The luminosity only depends on the machine parameters and can be written as

$$\mathcal{L} = \mathrm{f_{rev}} \cdot \mathrm{n_b} \cdot \frac{\mathrm{N_b^2}\gamma}{4\pi\epsilon\beta^*} \cdot \mathrm{F}, \tag{3.2}$$

assuming a Gaussian beam distribution. Here, $\mathrm{f_{rev}}$ is the revolution frequency, while $\mathrm{n_b}$ is the number of bunches. N_b is the number of particles per bunch, γ the Lorentz gamma, ϵ is the normalised emittance of the beam and β^* is the beta function, which describes the narrowness of the beam at the collision point. The function F accounts for the angle of the colliding beams.

Maximizing the instantaneous luminosity increases the collision rate and thus the data available. Accumulation of the instantaneous luminosity over a period of time yields the integrated luminosity:

$$\mathcal{L}_{\text{int}} = \mathcal{L} = \int \mathcal{L} \mathrm{dt} \tag{3.3}$$

3.2 The ATLAS detector

The ATLAS (A Toroidal Lhc ApparatuS) detector is a multi-purpose particle physics detector which covers the investigation of proton-proton collisions as well as heavy ion collisions. With a weight of approximately 7000 tons, a diameter of 25 m and a length of 44 m it is the largest detector of four detectors for particle physics at LHC. Its cylindrical geometry with one end-cap on each side to ensure full coverage in solid angle is built around interaction point (IP) one of the LHC beams. A schematic view of the ATLAS detector is given in Figure 3.2.

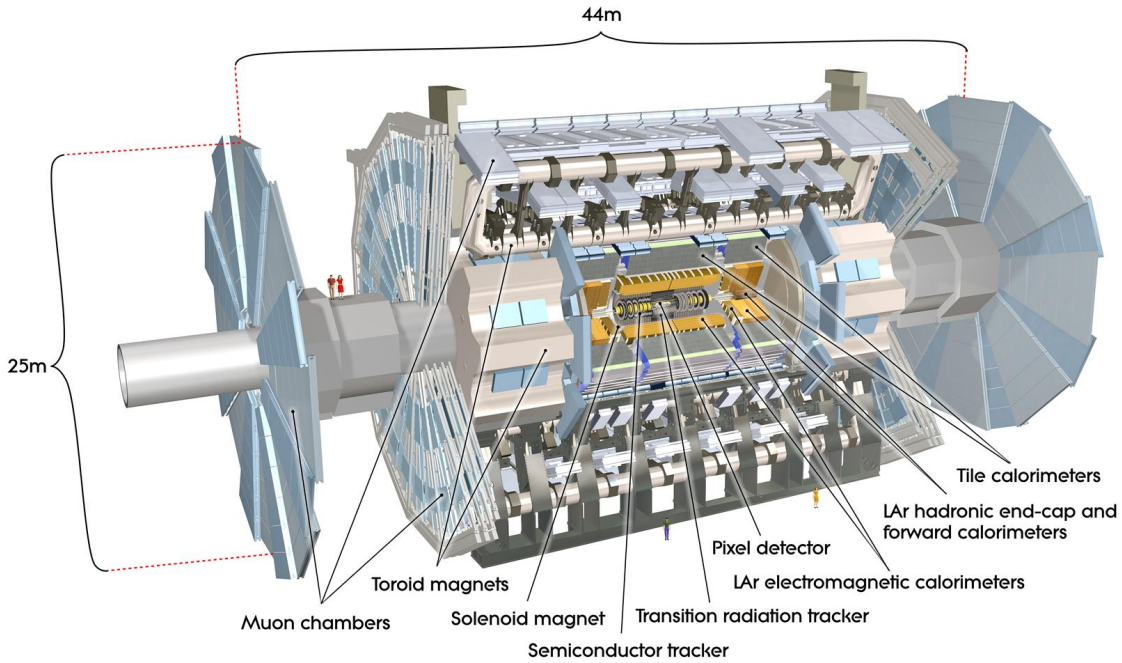

Fig. 3.2: Schematic view of the ATLAS detector ©CERN [26].

Apart from the magnet system, the ATLAS detector has three main parts, each comprising several subdetectors:

- **Inner detector:** Containing the pixel detector, the semiconductor tracker (SCT) and the transition radiation tracker (TRT).
- **Electromagnetic and hadronic calorimeter:** With Liquid Argon (LAr) and Tile subdetectors.
- **Muon spectrometer:** Made of various drift chambers to record the muon track.

Both the inner detector and the muon spectrometer have separate magnetic fields, a solenoidal field of 2 T for the inner detector and a toroidal field of up to 4 T for the outer detector. The large coils of the toroidal field of the outer magnet system define the characteristic appearance of the ATLAS detector.

The detector is able to precisely trace tracks of charged particles and determine the depleted energy. A schematic view of the particle signatures in the detector of the ATLAS experiment is illustrated in Figure 3.3.

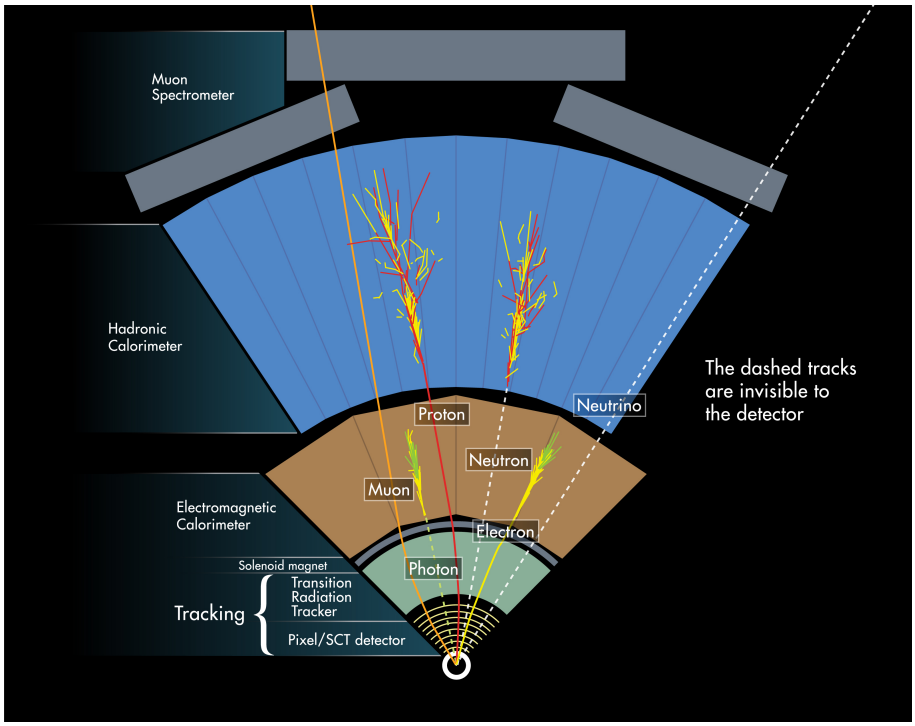

Fig. 3.3: Particle signatures in the detector of the ATLAS Experiment ©CERN [27].

3.3 The ATLAS coordinate system

The geometric and kinematic quantities analysed in this study are expressed by the coordinate system of the ATLAS detector with its origin at the nominal IP in the geometrical centre of the detector. A schematic view is given in Figure 3.4.

According to the Cartesian coordinate system, the z-axis is defined along the beam direction, while the x-y plane is transverse to it. In particular the x-axis points from the IP to the centre of the LHC ring, the y-axis is defined positive upwards while the z-direction is positive in the anti-clockwise direction of the LHC ring so that the coordinate system becomes right-handed.

Due to the shape of the ATLAS detector an equivalent description is expressed in Polar coordinates r and ϕ in conjunction with the z-coordinate. Thereby the azimuthal angle $\phi \in [0, 2\pi]$ is the angle around the beam axis. The polar angle $\theta \in [-\frac{\pi}{2}, \frac{\pi}{2}]$ is the angle with respect to the z-axis. In order to obtain Lorentz invariance, the pseudorapidity η is introduced, which corresponds to the polar angle θ:

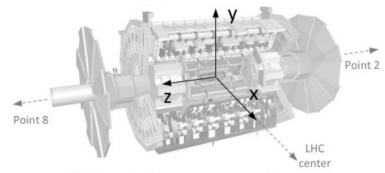

x-y-z right-handed Cartesian coordinate system

(a)

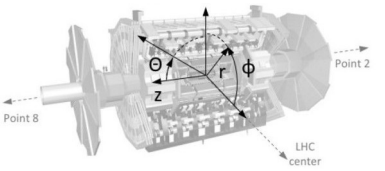

r-ϕ-z cylindrical coordinates and **Θ** - visualization

(b)

Fig. 3.4: Cartesian (a) and cylindrical (b) representation of the ATLAS coordinate system ©CERN [26], modified.

$$\eta = -\ln \tan\left(\frac{\theta}{2}\right). \tag{3.4}$$

For high energetic particles ($p \gg m$) the pseudorapidity η is equal to the rapidity y:

$$y = \frac{1}{2} \ln\left(\frac{E + p_z c}{E - p_z c}\right). \tag{3.5}$$

The angular distance ΔR between two particles denotes particle track distances in terms of pseudorapidity and azimuthal angle:

$$\Delta R = \sqrt{\Delta\eta^2 + \Delta\phi^2}. \tag{3.6}$$

The particles emerging from proton-proton collisions are described by momentum

and energy which are projected to the transverse plane [1]. The transverse momentum p_T, the transverse energy E_T and the missing transverse energy E_T^{miss} are defined as follows :

$$p_T = \sqrt{p_x^2 + p_y^2}, \tag{3.7}$$

$$E_T = E \cdot \sin\phi, \tag{3.8}$$

$$E_T^{miss} = \sqrt{E_x^{miss} + E_y^{miss}}. \tag{3.9}$$

[1] Particle properties denoted with the subscript T refer to the transverse (x-y) plane.

4 Event simulation and data analysis

This chapter describes the simulation of the $t\bar{t}\gamma$ process, both for the $t\bar{t}\gamma$ production process and for the $t\bar{t}\gamma$ total process including production and decay.

4.1 Data analysis chain

For analysing data provided by the ATLAS experiment, simulations of physics processes are necessary. SM predictions, also extensions or beyond SM (BSM) models can be implemented. Deviations between the simulation and the measured distributions need to be carefully studied since observed differences could either be related to a mismodelling in the simulation, e.g. parameters that need further tuning or missing higher order corrections, or effects from new physics beyond the SM. The simulation includes events which are generated by Monte Carlo (MC) event generators. In order to precisely predict the physics processes, a MC generator simulates interaction of particles, their decay with accurate branching ratios (parton level) and the interaction with the detector material (reconstruction level). The MC is generated in different steps. The physics model, i.e. SM, describes the framework in which the calculation is performed. The actual process is selected by defining the input and output particles as well as the order of calculation. The matrix element or the expression of the process probability is automatically prepared based on the physics model data. The samples used in this thesis are calculated at leading-order (LO) and next-to-leading-order (NLO), which describe the theoretical calculations of matrix elements in the physics process. Figure 2.3 depicts a LO diagram of the production of a $t\bar{t}$ pair via gluon fusion or quark annihilation. NLO diagrams offer one of two possible additions to the LO diagram, i.e. an extra emission or an extra loop, which is illustrated for $t\bar{t}$ pair production via quark annihilation in Figure 4.1 below.

After integration of the matrix element over the parameter phase space, the code for an event generator is constructed and will generate random samples of energy-momentum four-vectors for all final state physical particles. Each particle is then propagated into a model representing the experiment built by a detector simulation package.

(a) **(b)**

Fig. 4.1: QCD NLO diagrams for the production of a $t\bar{t}$ pair via quark annihilation with extra real emission (a) and extra loop (b).

The simulated data now, can be compared to the experimental data produced in the particle collisions, measured by the detector. Both simulation and data are then reconstructed by the same reconstruction programme to get the initial set of energy-momentum four-vectors representing the actual simulated or observed event. Comparing the reconstructed simulated four-momenta to those produced by the event generator is a test of self-consistency of the whole system although departure between the simulated and the experimental data may give hints to improve modelling even so to new physics discoveries. The final analysis can be performed with the ROOT data analysis toolkit, developed at CERN. This is how plots in this study have been produced, supplemented by the Rivet MC analysis framework.

4.2 Simulated datasets

In order to investigate the entire $t\bar{t}\gamma$ process, two MC samples employed in Reference [8] are used, one for the $t\bar{t}\gamma$ production process and one for the total $t\bar{t}\gamma$ process including production and decay. Furthermore, an additional sample was generated. The settings related to the dedicated samples used in the MC analysis are introduced below.

The information related to the modelling of the $t\bar{t}\gamma$ processes relies on Reference [8]. Both samples, $t\bar{t}\gamma$ production and decay were simulated with the same version of MadGraph5_aMC@NLO generator [28; 29] interfaced to Pythia 8 [30], using the A14 set of tuned parameters and the NNPDF3.0NLO PDF set [31]. The renormalisation scale μ_R and factorisation scales μ_F are dynamic and correspond to half of H_T, defined as

$$\mu_R = \mu_F = \frac{H_T}{2}, \quad H_T = \sum_i \sqrt{m_i^2 + p_{T,i}^2}\,, \tag{4.1}$$

where m_i and $p_{T,i}$ are the masses and transverse momenta of the particles generated from the matrix element calculation which determines LO, NLO respectively. Phase space cuts

are applied on the matrix-element level to avoid infrared and collinear singularities due to the photon radiation. Leptons and quarks at the matrix-element level are required to have a minimum p_T of 20 GeV and 1 GeV, respectively. In both samples, photons were required to have p_T =15 GeV and to be isolated according to a smooth-cone hadronic isolation criterion with $\delta_0 = 0.1, \epsilon_\gamma = 0.1$ and n = 2. These parameters are related to the so called Frixione isolation [32], which avoids infrared divergences. The heavy-flavour hadron decays were modelled by the Monte Carlo event generator EvtGen [33].

In detail, the $t\bar{t}\gamma$ production MC sample with the photon produced from the off-shell top quark or from initial-state radiation is simulated as a $2 \to 3$ process at NLO accuracy in QCD. In the process the on-shell top quarks in the final state are being decayed at LO using MadSpin [34; 35] to preserve spin correlations. Since $t\bar{t}\gamma$ production is characterised by containing events with the photon produced from the top quark or from initial-state radiation, the sample allows for interference effects between initial-state photon radiation from incoming partons and the final-state photon radiation from off-shell top quarks.

The MC sample of $t\bar{t}\gamma$ decay, where the photon arises from any of the decay products of the top quarks or from one of the on-shell top quarks, is a simulation at LO precision as a $2 \to 2$ process. The following decay of the top quarks corresponds to LO precision, also generated with MadGraph5_aMC@NLO.

Overall the $t\bar{t}\gamma$ production sample is normalised to the NLO cross-section given by the MC simulation. Since the $t\bar{t}\gamma$ decay sample is a LO sample, a NLO/LO inclusive k-factor of 1.5 obtained in Reference [36] is used to correct the normalization of the $t\bar{t}\gamma$ decay sample.

For the total $t\bar{t}\gamma$ production and decay process a simulation of $t\bar{t}\gamma$ as a double resonant $2 \to 7$ process performed at LO in QCD is used [37]. The diagrams where the photon is radiated from the initial state, from the intermediate top quarks, b-quarks, the intermediate W bosons, and from the decay products of the W bosons, are included. This $t\bar{t}\gamma$ MC sample is generated using MadGraph5_aMC@NLO interfaced with NNPDF2.3LO PDF set [28] and Pythia 8. Since the MC sample for the $t\bar{t}\gamma$ total process is a LO MC sample, it is scaled to NLO prediction using the k-factor derived in [37].

As part of this study an additional MC sample was generated with limited cuts at generator level, i.e. with a minimum photon p_T of 15 GeV but no cuts on the decay products of $t\bar{t}$, in order to simulate the full phase space of the $t\bar{t}$ system. An extract of the configuration file with the corresponding conditions can be found in the appendix A.1. Accordingly, the minimum p_T for charged leptons was set to zero as well as the minimum p_T for the jets and the minimal invariant mass of same flavour lepton pair. In the same way no cuts were chosen for the maximum rapidity for the charged leptons.

5 Measurement of inclusive and differential cross sections of $t\bar{t}\gamma$ process

This chapter briefly introduces the analysis performed on $t\bar{t}\gamma$ production published in Reference [8]. The studies presented in this thesis were developed according to this measurements. Summarising the original analysis, this chapter ends with an overview of the results used for comparisons.

5.1 Introducing the reference measurement

The measurements in Reference [8] provide the cross section of the $t\bar{t}\gamma$ production process, where the photon is radiated from one of the incoming quarks, or the top quark, for the first time. The measurements are performed in single-lepton and dilepton $t\bar{t}$ channels at stable particle level in a fiducial phase space with the goal to estimate the inclusive and differential cross section for the production mode of a top quark pair $t\bar{t}$ in association with a photon γ.

As described in chapter 2.3, the photon can originate not only from an incoming charged parton or from an off-shell top quark, but also from its charged decay products, including a charged fermion from the decay of the W-boson. In previous analyses published by the ATLAS experiment at 13 TeV [38] or the CMS experiment at 13 TeV [39; 40] criteria were applied to suppress those radiated from top-quark decay products, e.g. by requiring the photon to have a large angular distance from the lepton(s). But no attempt was made to separate the different sources of photons.
Following Reference [8] the analysis strategy is designed to improve the separation of the $t\bar{t}\gamma$ production events as signal from the $t\bar{t}\gamma$ decay as background. The samples used for the analysis consist of data samples measured with the ATLAS detector and MC samples for the signal process as well as MC simulation and data-driven methods for the different background processes, which are categorized on the basis of photon origin.

The data sample was collected with the ATLAS detector at the LHC during Run 2 between 2015 and 2018 with $\sqrt{s} = 13$ TeV in proton-proton collisions corresponding to an integrated luminosity of 140 fb^{-1}.

The simulated MC samples used have already been described in section 4.2.

The separation of $t\bar{t}\gamma$ production and $t\bar{t}\gamma$ decay is intended to improve the measurement accuracy of the inclusive and differential cross section and to expand the studies of the $t\bar{t}\gamma$ production properties. The $t\bar{t}\gamma$ events where the photons are radiated from any of the charged decay products are expected to be the largest prompt photon background.

Although the focus of the analysis is on $t\bar{t}\gamma$ production process as signal, for completeness the cross sections are also measured including the $t\bar{t}\gamma$ decay process as part of the signal.

5.2 Inclusive cross section measurements

The following section presents a summary of the inclusive cross section measurements of Reference [8] relevant for comparing within the studies of this thesis. Here the focus is on $t\bar{t}\gamma$ production excluding $t\bar{t}\gamma$ decay as background.

The fiducial $t\bar{t}\gamma$ production cross-section in the single-lepton channel predicted by MadGraph5_aMC@NLO interfaced to Pythia 8 [8] is

$$\sigma^{\text{Single-lepton}}_{t\bar{t}\gamma \text{ production,MC}} = 255^{+25}_{-26} \text{ (scale)}^{+6}_{-4} \text{ (PDF) fb}, \tag{5.1}$$

and, in the dilepton channel is

$$\sigma^{\text{Dilepton}}_{t\bar{t}\gamma \text{ production,MC}} = 40.9^{+3.9}_{-4.0} \text{ (scale)}^{+6}_{-4} \text{ (PDF) fb}. \tag{5.2}$$

Accordingly, the expected cross section for the combination of single-lepton and dilepton channels generated by the NLO MadGraph5_aMC@NLO simulation is

$$\sigma^{\text{Combined}}_{t\bar{t}\gamma \text{ production,MC}} = 296\ ^{+29}_{-30} \text{ (scale)}\ ^{+6}_{-4} \text{ (PDF) fb}. \tag{5.3}$$

The measured $t\bar{t}\gamma$ production cross section in combined single-lepton and dilepton channels [8] results

$$\sigma_{t\bar{t}\gamma \text{ production}} = 319 \pm 15 \text{ fb} = 319 \pm 4 \text{ (stat)}\ ^{+15}_{-14} \text{ (syst) fb}. \tag{5.4}$$

5.3 Differential cross section measurements

The measurement of the differential cross section is done for $t\bar{t}\gamma$ production and the total $t\bar{t}\gamma$ process including photons from production and decay. Both absolute and normalised cross sections are measured in single-lepton and dilepton channels.

The list of relevant variables measured differentially is specified in Table 5.1 and comprises photon, lepton and jet kinematic variables just as angular separations of the photon, lepton and jets for both channels. Since the kinematic properties and angular separations have significant shape differences between $t\bar{t}\gamma$ production and $t\bar{t}\gamma$ decay, which has already been covered in section 2.3, they are estimated for both $t\bar{t}\gamma$ processes separately. Additional differential distributions of leptonic variables are measured in dilepton channel for the $t\bar{t}\gamma$ total process. The photon p_T and $|\eta|$ distributions are measured in each channel and in the combined single-lepton and dilepton channels.

Variable	**Description**
	Both channels
$p_T(\gamma)$	Transverse momentum of the photon
$\lvert\eta(\gamma)\rvert$	Absolute value of pseudorapidity of the photon
$\Delta R(\gamma,\ell)_{min}$	Angular separation between the photon and the closest lepton
$\Delta R(\gamma,b)_{min}$	Angular separation between the photon and the closest b-jet
$\Delta R(\ell,j)_{min}$	Smallest angular separation between any of the selected leptons and jets
$p_T(j_1)$	Transverse momentum of leading jet in p_T
	Additional variables: dilepton channel
$\Delta R(\gamma,\ell_1)$	Angular separation between the photon and the leading lepton
$\Delta R(\gamma,\ell_2)$	Angular separation between the photon and the subleading lepton
$\lvert\Delta\eta(\ell,\ell)\rvert$	Pseudorapidity difference between the two leptons
$\Delta\phi(\ell,\ell)$	Azimuthal angle difference between the two leptons
$p_T(\ell,\ell)$	Transverse momentum of the dilepton system

Tab. 5.1: List of kinematic variables measured differentially in the single-lepton and dilepton channels.

The motivation to choose the above variables, is based on the fact that the kinematic properties of the photon are sensitive to the top-photon coupling, especially the photon p_T. The angular separations ΔR_{min} are related to the angle between the top quark and the radiated photon which give insight into the structure of this coupling and are expected less sensitive to the top quark off-shell effects [41]. The additional differential distributions of leptonic observables specified in the dilepton channel for $t\bar{t}\gamma$ total process are of interest due to their sensitivity to the $t\bar{t}$ spin correlation, following the references [42; 43]. In particular $\Delta\phi(\ell,\ell)$ and $|\Delta\eta(\ell,\ell)|$ are focused here.

A summary of the differential cross section measurements of Reference [8], which are relevant for the comparison in the context of the studies of this thesis, are depicted below.

5.3.1 Differential distributions for the $t\bar{t}\gamma$ production process

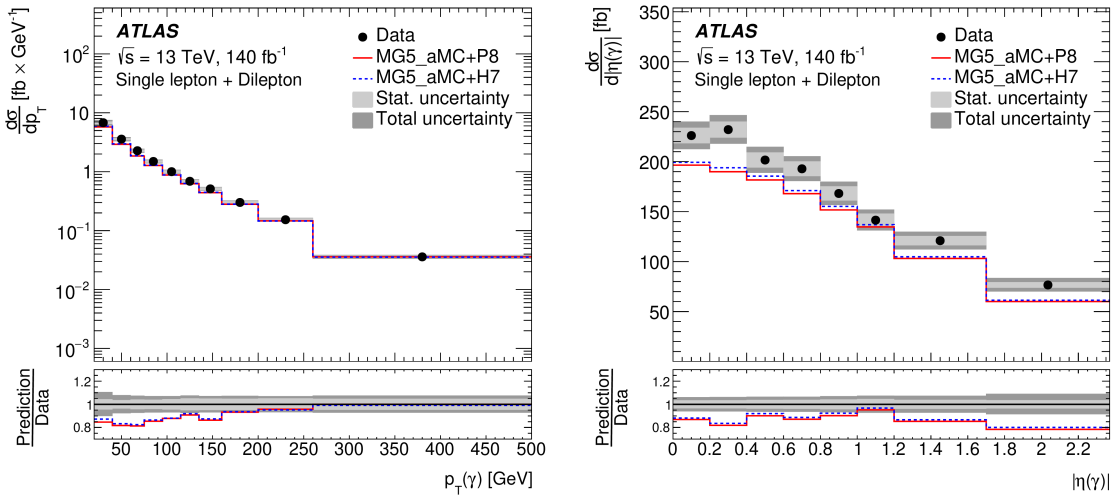

(a) (b)

Fig. 5.1: Absolute $t\bar{t}\gamma$ production differential cross sections measured in the combined fiducial phase space of the single-lepton and dilepton channels as a function of the photon p_T (a) and $|\eta|$ (b). The last bin of the $p_T(\gamma)$ distribution includes the overflow events [8].

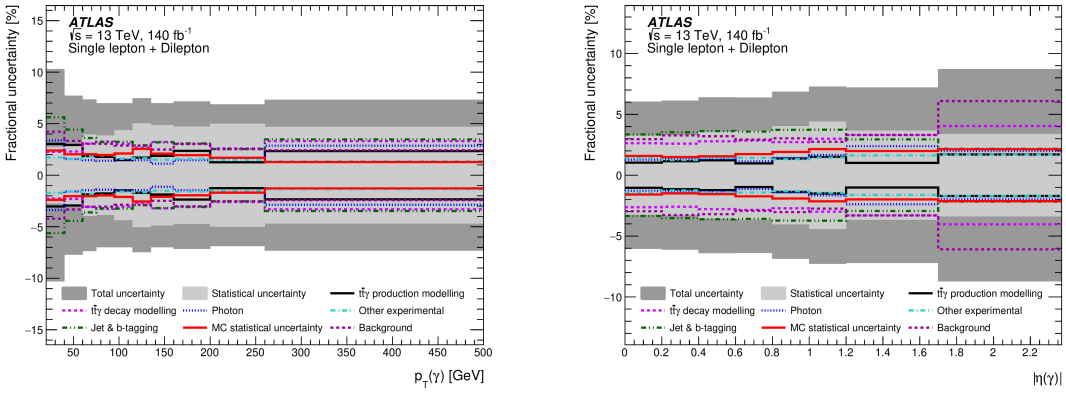

(a) (b)

Fig. 5.2: Contributions of the systematic uncertainties grouped in categories of the absolute $t\bar{t}\gamma$ production differential cross-sections measured in the combined fiducial phase space of the single-lepton and dilepton channels as a function of the photon p_T (a) and $|\eta|$ (b) [8].

Figur 5.1 depicts the absolute $t\bar{t}\gamma$ production differential cross sections measured in the combined fiducial phase space of the single-lepton and the dilepton channels as a function of the photon p_T and $|\eta|$. In section 7.1 the measured data of Figure 5.1 is used for extrapolating to the measured total phase space of the $t\bar{t}$ system.

The percentage contributions of systematic uncertainties and the statistical one grouped by categories are shown in Figure 5.2. The total uncertainty varies up to 10 %. The main contribution comes from the experimental uncertainties related to jet uncertainties as well as b-tagging uncertainties.

5.3.2 Differential distributions for the $t\bar{t}\gamma$ total process

For completeness, selected differential distributions for $t\bar{t}\gamma$ total are listed in Figure 5.1, since the $t\bar{t}\gamma$ total $2 \rightarrow 7$ MC sample is used for validation in chapter 6.

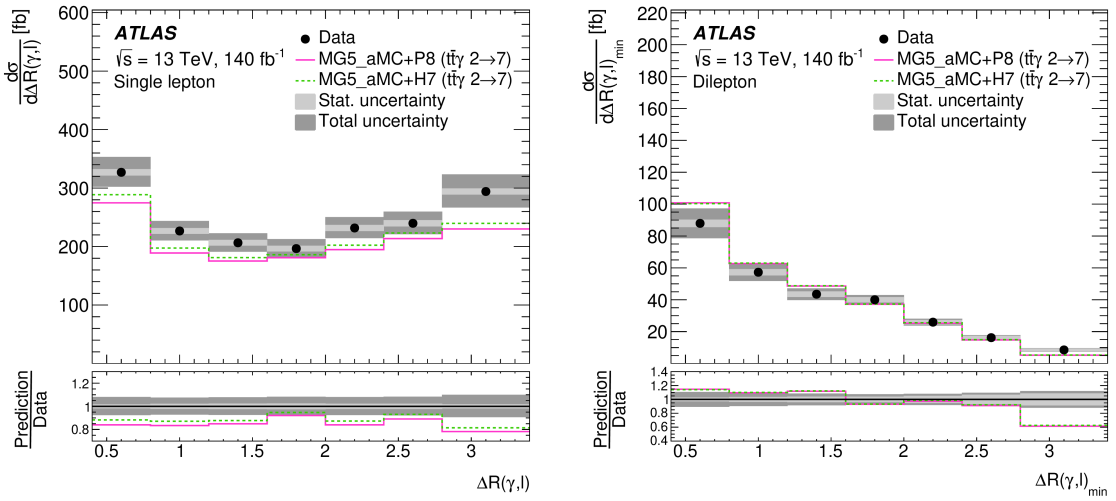

(a) **(b)**

Fig. 5.3: Absolute $t\bar{t}\gamma$ total differential cross sections in the fiducial phase space of single-lepton (a) and dilepton (b) channels as a function of $\Delta R(\gamma, l)$ [8].

6 The Rivet MC analysis framework

Within this study a Rivet routine for Reference [8] was developed and validated. The following sections describe the development of the routine for the $t\bar{t}\gamma$ production as well as the total $t\bar{t}\gamma$ production and decay processes. The analysis is done at stable particle level in a fiducial region focussing on single-lepton and dilepton $t\bar{t}$ decay channels as well as the combination.
The published Rivet routine can be found in Reference [7].

6.1 Motivation

RIVET is a C^{++} and python-based analysis framework whose acronym stands for **R**obust **I**ndependent **V**alidation of **E**xperiment and **T**heory. It provides the most widespread way by which analysis code from high-energy collider experiments is preserved and especially is used for comparison to and development of further theory models, i.e. MC generator development, validation and tuning.

The aim of this master's thesis was to provide the code mimicking the definitions of the fiducial phase space at particle level used in the Reference [8]. As a key aspect this allows to compare simulations and future calculations with the measurement in a convenient way.

6.2 Object and event selection with Rivet

In order to select the correct events for the $t\bar{t}\gamma$ production and $t\bar{t}\gamma$ total process, an event selection has been developed, which allows to compare the results to the data and simulation used in Reference [8]. For the remaining requirements in the event selection, the values were chosen to be identical as in Reference [8].

6.2.1 Particle level object definition

The following part of the section describes how the physics objects are selected. The full selection is done at particle level. The use of particle level definitions common across experiments and theory facilitate comparisons. A suitable definition is based on stable particles, a collection of objects that are considered stable in MC simulation, i.e. for the lifetime τ applies $\tau > 30$ ps. Simulations of the interaction of these particles with the detector components or additional proton-proton interactions are not included.

The objects of interest in this thesis are photons, leptons, particle-level jets, b-jets and missing transverse momentum E_T^{miss}, i.e. neutrinos. In the following the objects at particle level are defined.

Isolation requirement
Every particle should be isolated without being mixed up with other particles. Only particles which pass the kinematic requirements of the object selection are considered.

Object selection

- **Photons**
  Photons are required to not originate from a hadron decay, satisfying $p_T > 20$ GeV and $|\eta| < 2.37$. In addition the photon has to be isolated, i.e. the sum of transverse momenta of all charged particles surrounding the photon within $\Delta R \leq 0.2$ is less than 5% of its own p_T.

- **Leptons**
  Leptons are required to have $p_T > 25$ GeV and $\eta < 2.5$, and must not originate from hadron decays. Electron and muons are "dressed" with nearby photons within a $\Delta R = 0.1$ cone around the lepton. The momenta of the nearby photons are added to the lepton before applying the selection. The τ leptons are not discussed explicitly as particle level objects, but their leptonic decay products are considered.

- **Particle-level jets**
  Jets are defined by a jet algorithm that clusters a set of particles. The jet algorithm used to be infra-red and collinear safe. Particle-level jets are clustered with the anti-k_t algorithm with a distance parameter of $R = 0.4$. All stable particles are considered in the clustering, except for the selected electrons, muons and photons, and the neutrinos originating from top quarks. Jets are required to satisfy $p_T > 25$ and $|\eta| < 2.5$.

- **b-jets**
  Jets that originate from b-quarks are called b-jets. A jet is identified as a b-jet if a hadron with $p_T > 5$ containing a b-quark is matched to the jet via a ghost-matching method [45].

Overlap removal
Jet activities close to leptons are prone to double-counting of jets and leptons. Therefore, an overlap removal is applied, which differs for leptons and photons. In order to preserve as many events as possible, it is important to choose the correct order of the procedure given as follows:

- Muons and electrons with separation $\Delta R(\ell, j) < 0.4$ from a jet are excluded.
- Jets are removed if they are within $\Delta R(j, \gamma) = 0.4$ of an isolated photon candidate.
- Events are required to satisfy $\Delta R(\gamma, \ell) > 0.4$, where ℓ stands for electron e or muon μ.

6.2.2 Event selection

This part of the selection summarises the fiducial phase space used to define the cross section since it filters single-lepton and dilepton $t\bar{t}\gamma$ events. Only events that pass the full selection contribute to the cross section. For the combination of the channels a union of single-lepton and dilepton fiducial phase space is used. A summary of the exact definitions of fiducial phase space for the single-lepton and dilepton channels can be found in Table 6.1.

Single-lepton channel	**Dilepton channel**
exactly one γ	exactly one γ
one lepton (e or μ)	two leptons (ee, eμ, $\mu\mu$)
at least four jets (with at least one jet b-tagged)	at least two jets (with at least one jet b-tagged)

Tab. 6.1: Summary of fiducial phase space definition for single-lepton and dilepton channel.

Furthermore, events with additional leptons satisfying $p_T > 7$ GeV are excluded.

6.3 Studies of selection requirements

This section briefly summarises the studies at particle level on development of the Rivet routine and shows that implementing precisely the cuts is relevant. The goal is to improve the signal as in the analysis in Reference [8]. The investigations that will be considered in more detail are related to the selection of the tau leptons, the impact of the jet-finding algorithm selection criteria and the finetuning, especially with regard to the leading jet.

6.3.1 Impact of including leptonic tau lepton decays

This section describes the effects of tau lepton decays in the Rivet routine calculations as tau leptons are not included by default for selection of final state particles directly connected to the hard process. Figure 6.1 shows the p_T distributions of the leading jet for $t\bar{t}\gamma$ production in single-lepton and dilepton channels comparing the effect of included or not included leptonic part of tau lepton decays. The distributions are calculated with a subset of the $t\bar{t}\gamma$ production MC sample using Rivet as this is a test of the increase of events by including the leptonically decaying tau leptons.

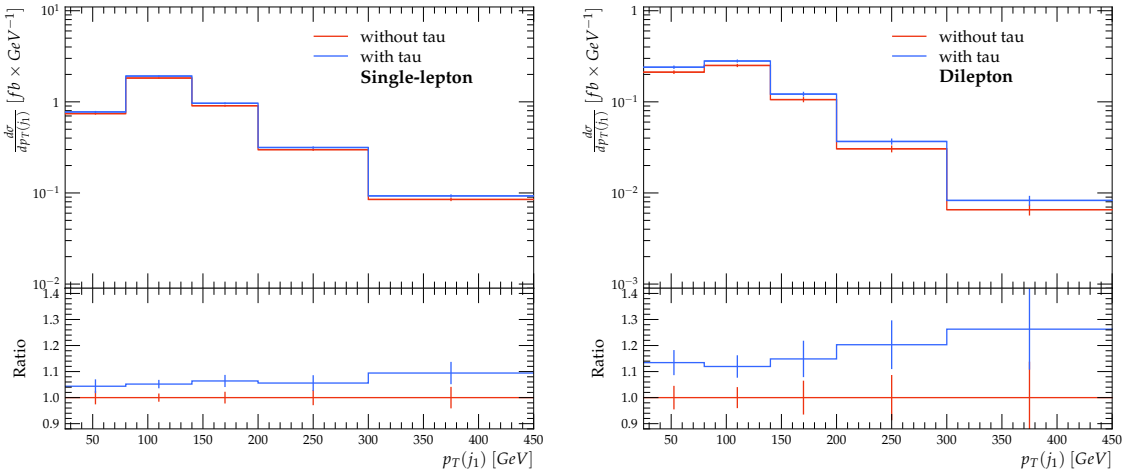

(a) **(b)**

Fig. 6.1: The leading jet particle level distribution $p_T(j_1)$ for $t\bar{t}\gamma$ production in single-lepton (a) and dilepton (b) channels of included tau lepton decays compared to non-included tau lepton decays calculated with the Rivet routine.

Including tau leptons for the selection of final state particles directly associated with the hard process increases the proportion of selected events. Thus, the implementation of the tau lepton decay leads to a higher accuracy of the calculations with the Rivet routine compared to the original analysis in Reference [8] which is shown in the following figures.

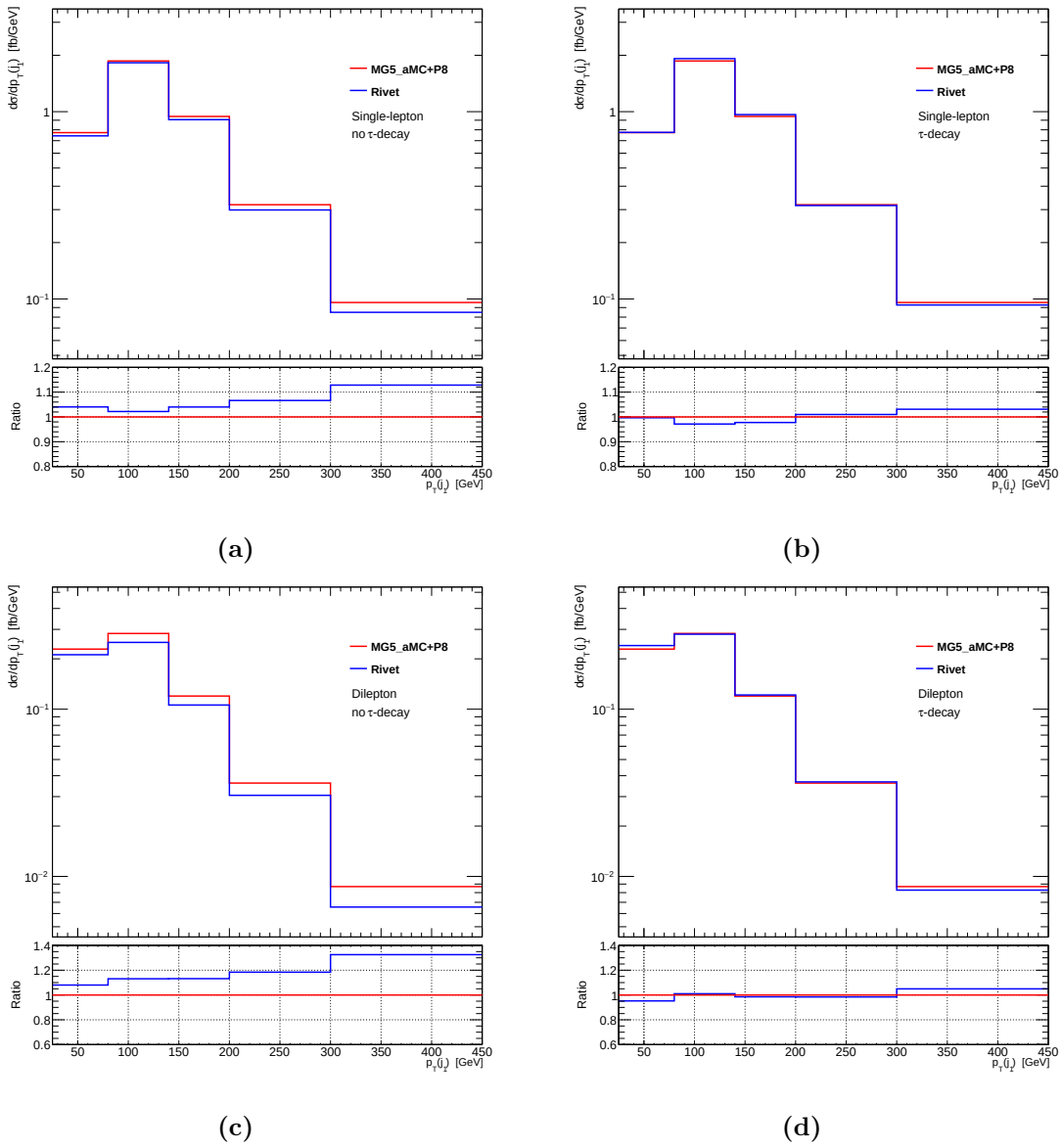

Fig. 6.2: The leading jet particle level distribution $p_T(j_1)$ for $t\bar{t}\gamma$ production in single-lepton and dilepton channels to compare the Rivet routine *(blue)* with (b, d) and without (a, c) implemented decay of the tau leptons in reference to the simulated original analysis *(red)*.

As can be seen in Figure 6.2b and Figure 6.2d implementing the decay of the tau lepton shifts the distribution of around 4% (8 %) in low p_T regions in single-lepton (dilepton) channel and around 10% (20 %) in higher p_T regions, respectively. The proportionality of about 2 between single-lepton and dilepton channel corresponds to the expectations. The inclusion of tau decays improves the result.

6.3.2 Jet definitions

In this section, the selection of the jet algorithm of the Rivet routine has been tested. Searching for jets with jet algorithms via the FastJet package provides an enumeration for the treatment of muons: whether to include all, some, or none in jet-finding [46]. Among the observables listed in the table 5.1, the leading jet is the most sensitive observable for the selection criteria.

Figure 6.3 shows the results for the different treatments of muons in the jet algorithm related to the leading jet.

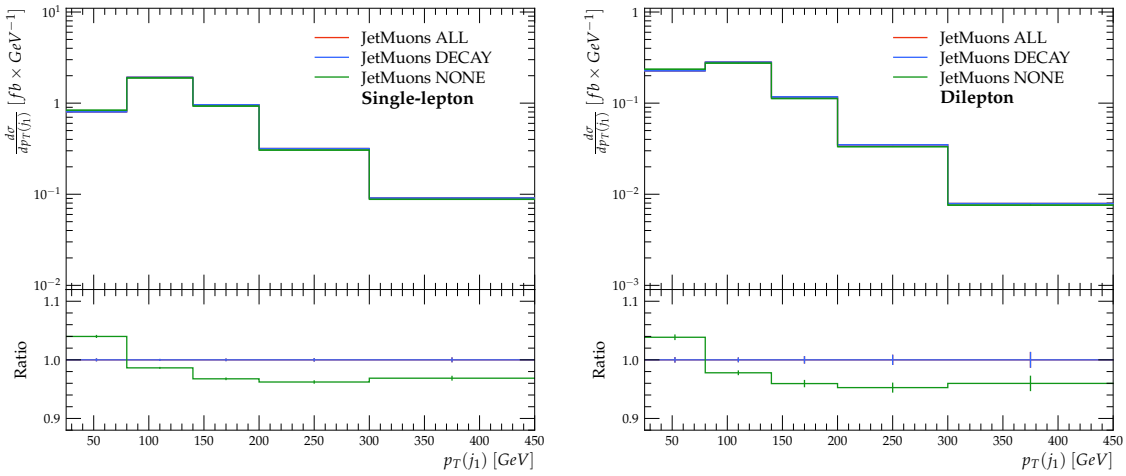

(a) **(b)**

Fig. 6.3: The leading jet particle level distribution $p_T(j_1)$ for $t\bar{t}\gamma$ production in single-lepton (a) and dilepton (b) channels determined by Rivet to compare the enumeration type for the treatment of muons: whether to include all, some, or none in jet-finding.

As illustrated in Figure 6.3, there is no difference in the treatment of including all or only some muons. However, neglecting all muons in the jet algorithm leads to a loss of events, especially for the leading jet. Examination of $p_T(\gamma)$ and $|\eta(\gamma)|$, or other jet-related observables shows only small deviations, see Figure 6.4 and Figure 6.5.

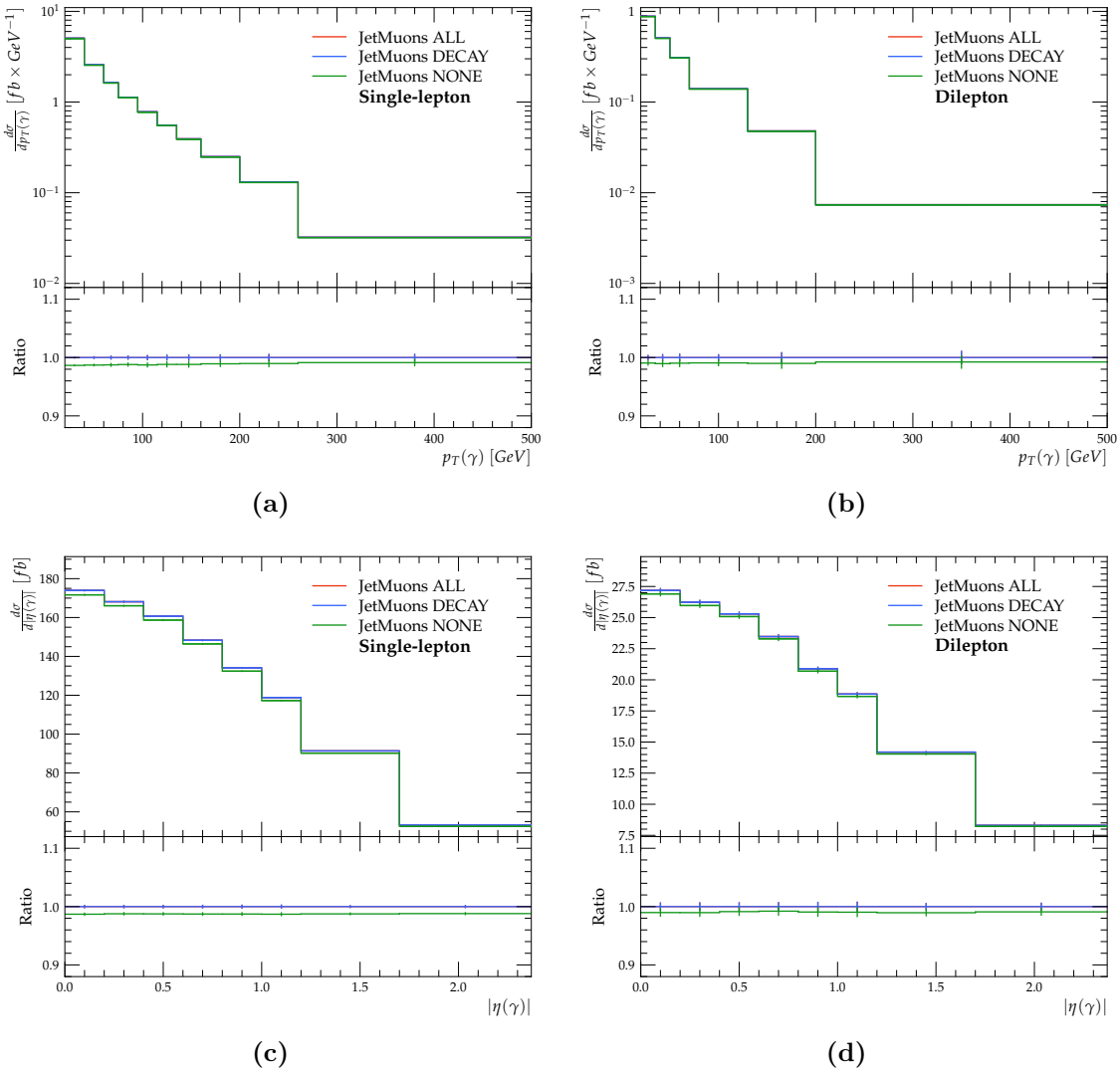

Fig. 6.4: Particle level distributions of $p_T(\gamma)$ and $|\eta(\gamma)|$ for $t\bar{t}\gamma$ production in single-lepton (a,c) and dilepton (b,d) channels to compare the enumeration type for the treatment of muons: whether to include all, some, or none in jet-finding.

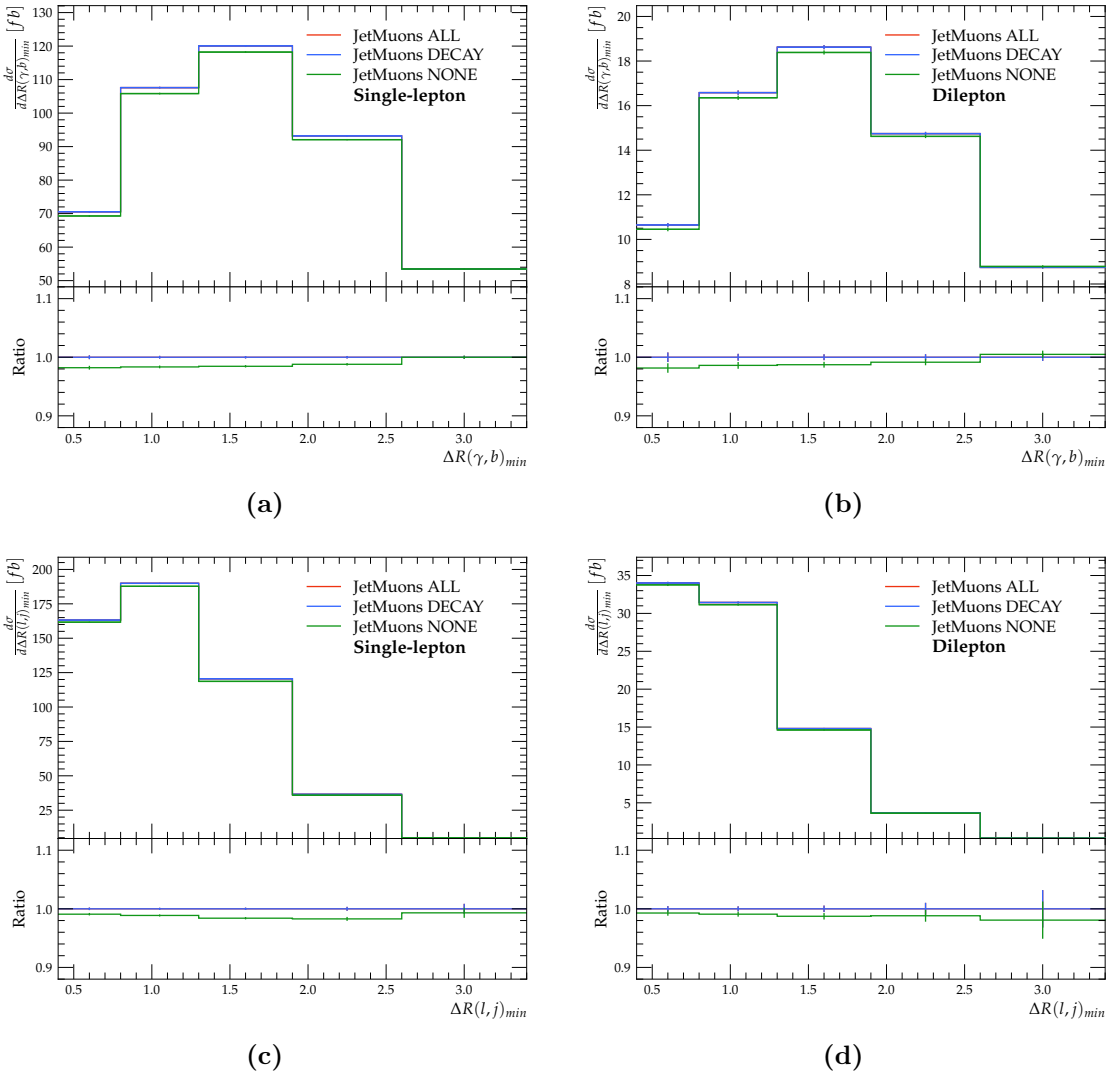

Fig. 6.5: Particle level distributions of ΔR(γ, b) and ΔR(l, j) for $t\bar{t}\gamma$ production in single-lepton (a,c) and dilepton (b,d) channels to compare the enumeration type for the treatment of muons: whether to include all, some, or none in jet-finding.

The effects of the included and neglected muons in the Rivet routine compared to the original original analysis [8] are shown in Figure 6.6. The inclusion of all muons in the jet-finding algorithm finally leads to an improvement of the code.

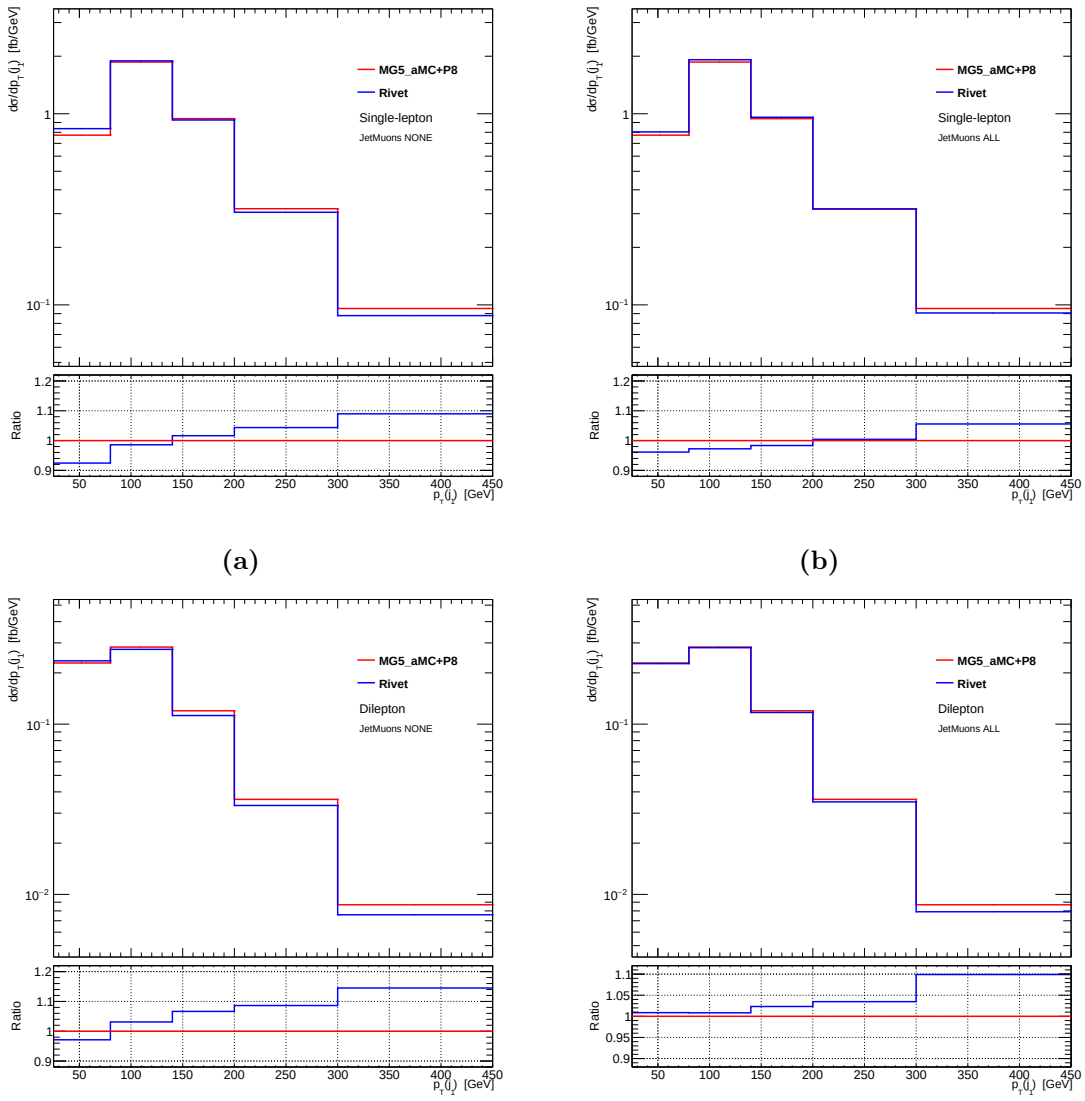

Fig. 6.6: The leading jet particle level distribution $p_T(j_1)$ for $t\bar{t}\gamma$ production in single-lepton (a,b) and in dilepton (c,d) channels. Comparison of all and none included muons in the jet-clustering between results of the Rivet routine and the original analysis [8].

6.3.3 Optimization of requirements

Several tests are applied to finalise the routine. Thus the order of the overlap removals has been tested and the discard of leptons with $\Delta R(\ell, j) < 0.4$ set before photon isolation. In addition, a $p_T(\gamma) > 20$ GeV requirement for selected photons is implemented in the code as well as no vetoed photons in the jet algorithm. Figure 6.7 shows an intermediate result for the routine, in which deviations of the leading jet p_T still remain, specifically related to the single-lepton channel.

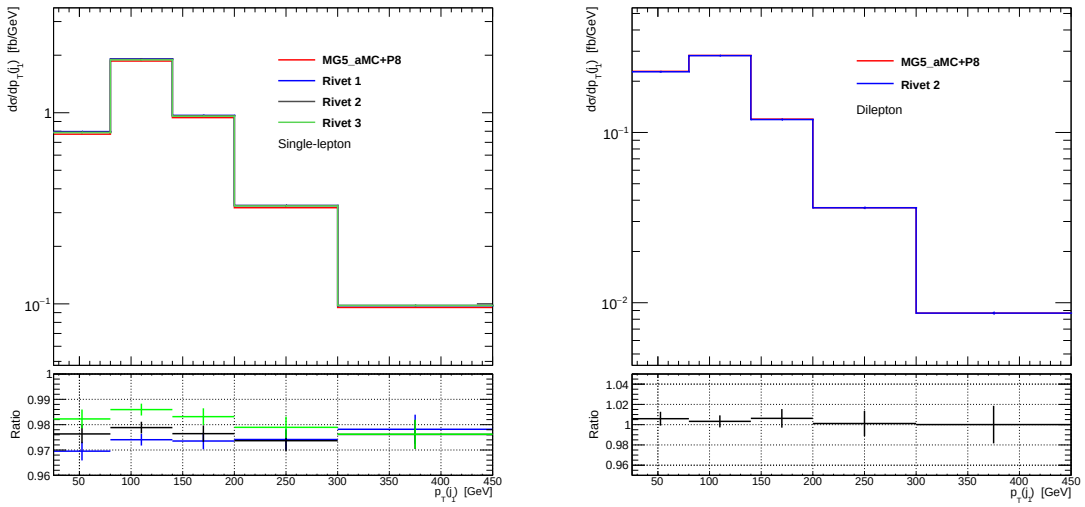

(a) **(b)**

Fig. 6.7: Differential distribution of $p_T(j_1)$ with included $p_T(\gamma) > 20$ and vetoed photons in the jet-algorithm *(blue)*, included $p_T(\gamma) > 20$ and no vetoed photons in the jet-algorithm *(black)*, and nor included $p_T(\gamma) > 20$ nor vetoed photons in the jet-algorithm *(green)* in the single-lepton channel (a). The results of the Rivet routine are compared to Reference [8] *(red)*. The optimized result is given by Rivet 2. The corresponding result for the dilepton channel is shown in b.

As can be seen in Figure 6.7a the distribution of the leading jet in single-lepton channel is shifted around 2 %. The corresponding distribution in the dilepton channel agrees well within statistical uncertainties. The following selection of plots illustrates that the deviation is related to the single-lepton channel only, see Figure 6.8.

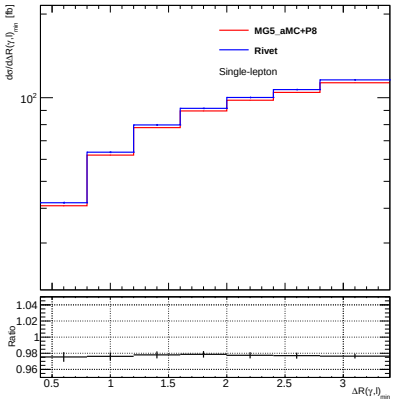

(a)

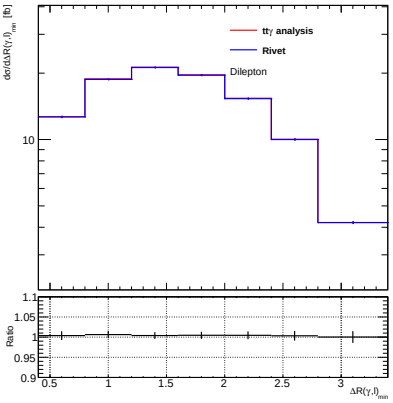

(b)

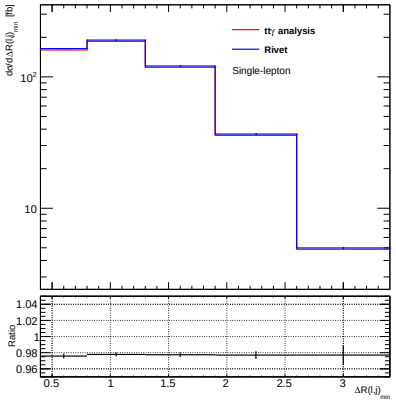

(c)

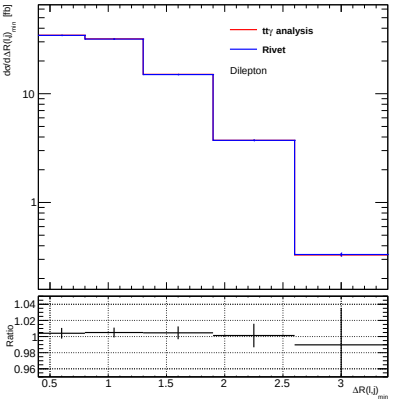

(d)

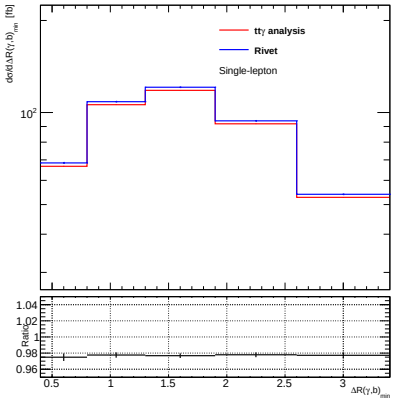

(e)

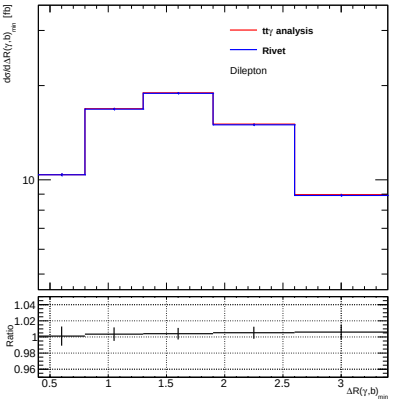

(f)

Fig. 6.8: Differential distributions for $\Delta R(\gamma, l)$, $\Delta R(\gamma, b)$ and $\Delta R(\ell, j)$ in single-lepton (a,c,e) and dilepton (b,d,f) channels compared to corresponding distributions in the original analysis [8].

In order to correct the selected events, additional leptons satisfying pT $>$ 7 GeV are excluded. This correction only affects the single-lepton channel. Since the event selection in higher p_T regions decreases as a result, the overlap removal of $\Delta R(l, j) < 0.4$ also is applied for the vetoed leptons that satisfy pT $>$ 7 GeV. The corrected distributions in comparison to the original analysis are illustrated for single-lepton channel in Figure 6.9a and Figure 6.9b, respectively.

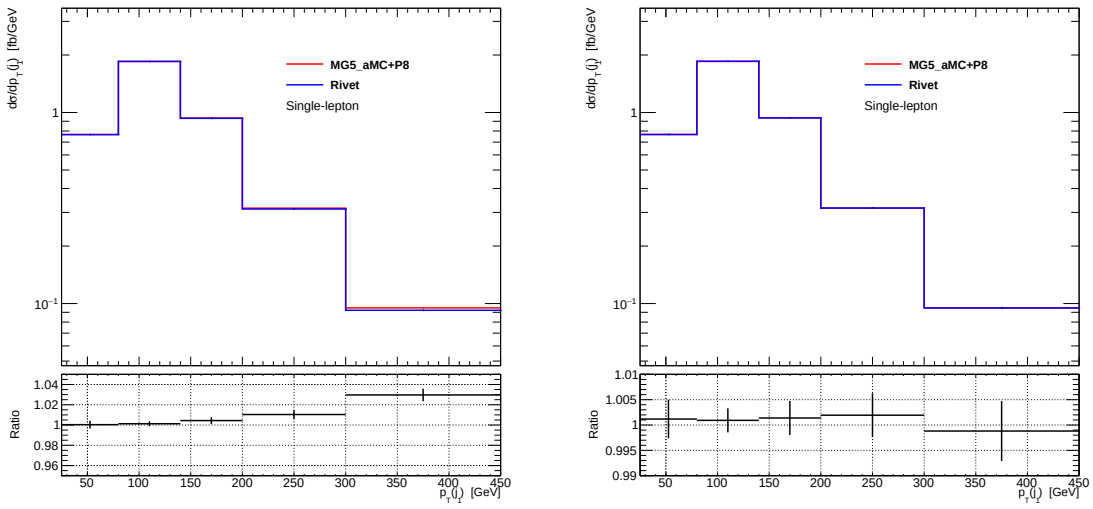

(a) **(b)**

Fig. 6.9: The leading jet particle level distribution $p_T(j_1)$ for $t\bar{t}\gamma$ production in single-lepton channel with applied requirement of excluded leptons satisfying pT $>$ 7 GeV (a) and additional implementation of the overlap removal $\Delta R(l, j) < 0.4$ for the vetoed leptons that satisfy pT $>$ 7 GeV (b).

6.4 Results

The following section presents the results produced with the developed Rivet routine for $t\bar{t}\gamma$ production as well as $t\bar{t}\gamma$ total process, compared to the corresponding distributions in Reference [8]. For comparison the same binning is used. Both absolute and normalised cross sections are compared. The ratio is defined as:

$$\text{Ratio} = \frac{\text{Prediction}}{\text{MC}},$$

where "Prediction" is the result of running the Rivet routine while "MC" corresponds to curves obtained with Reference [8]. The cross section distributions are obtained in the fiducial phase space discussed in section 6.2.2. The list of variables compared is shown in Table 5.1.

6.4.1 Absolute and normalised $t\bar{t}\gamma$ production differential cross-section in fiducial phase space

The following section specifies the results for $t\bar{t}\gamma$ production in single-lepton, dilepton and combined channels.

The kinematic distributions considered for $t\bar{t}\gamma$ production in the single-lepton and dilepton channels include $p_T(\gamma)$, $|\eta(\gamma)|$, $\Delta R(\gamma, \ell)_{\text{min}}$, $\Delta R(\gamma, b)_{\text{min}}$, $\Delta R(\ell, j)_{\text{min}}$ and $p_T(j_1)$. For the combined channel only $p_T(\gamma)$ and $|\eta(\gamma)|$ are determined and listed for completeness due to further examinations (see chapter 7). Both absolute and normalised differential cross sections are calculated. The last bin of the distributions related to the angular distances ΔR and the momentum p_T include the overflow events. The Rivet results are obtained from the NLO predictions of the MadGraph5_aMC@NLO simulation interfaced to Pythia 8 for $t\bar{t}\gamma$ production presented section 4.2 and also used in Reference [8].

Furthermore, the photon transverse momentum $p_T(\gamma)$ and the photon pseudorapidity $|\eta(\gamma)|$ are sufficient for illustration purposes in single-lepton (6.10), dilepton (6.11) and combined channels (6.12), unless otherwise stated. The distributions of the remaining kinematic quantities can be found in the appendix 8.

Overall the distributions are in good agreement. There are no significant differences between the results of the two codes for the simulation of $t\bar{t}\gamma$ production. The results of the Rivet routine describe the shape of the distributions well, especially for the single-lepton channel.

The differential cross-sections, absolute as well as normalised, are within the statistical uncertainty which is about 1‰ - 2‰ depending on the variable and the bin of the distribution.

Single-lepton channel

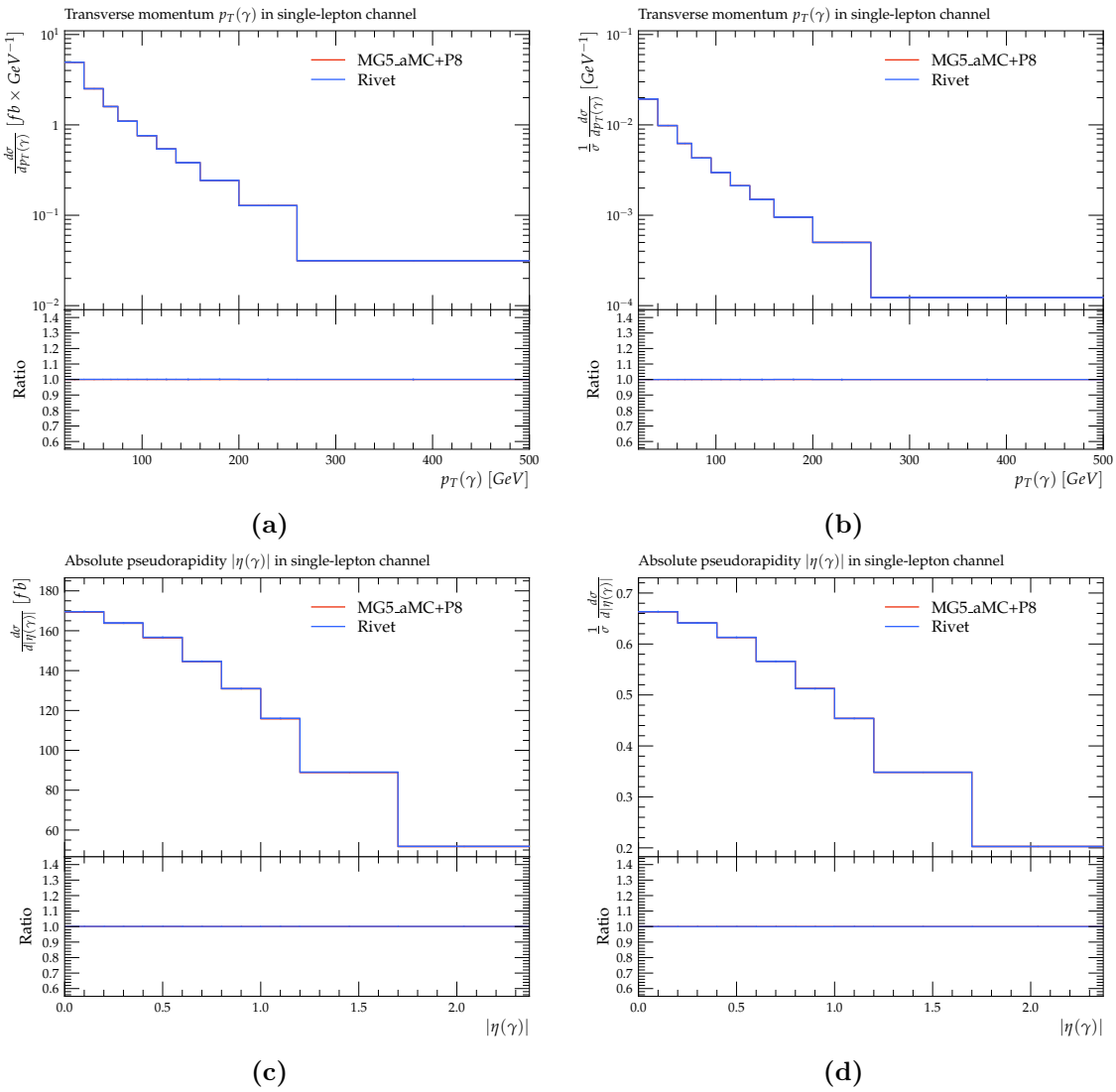

Fig. 6.10: Validation plots for $t\bar{t}\gamma$ production process. Comparison of the absolute (a,c) and normalized (b,d) cross section as a function of photon p_T (a,b) and photon $|\eta|$ (c,d) in the single-lepton channel, obtained with the Rivet routine *(blue)* and the analysis code *(red)* [8].

Dilepton channel

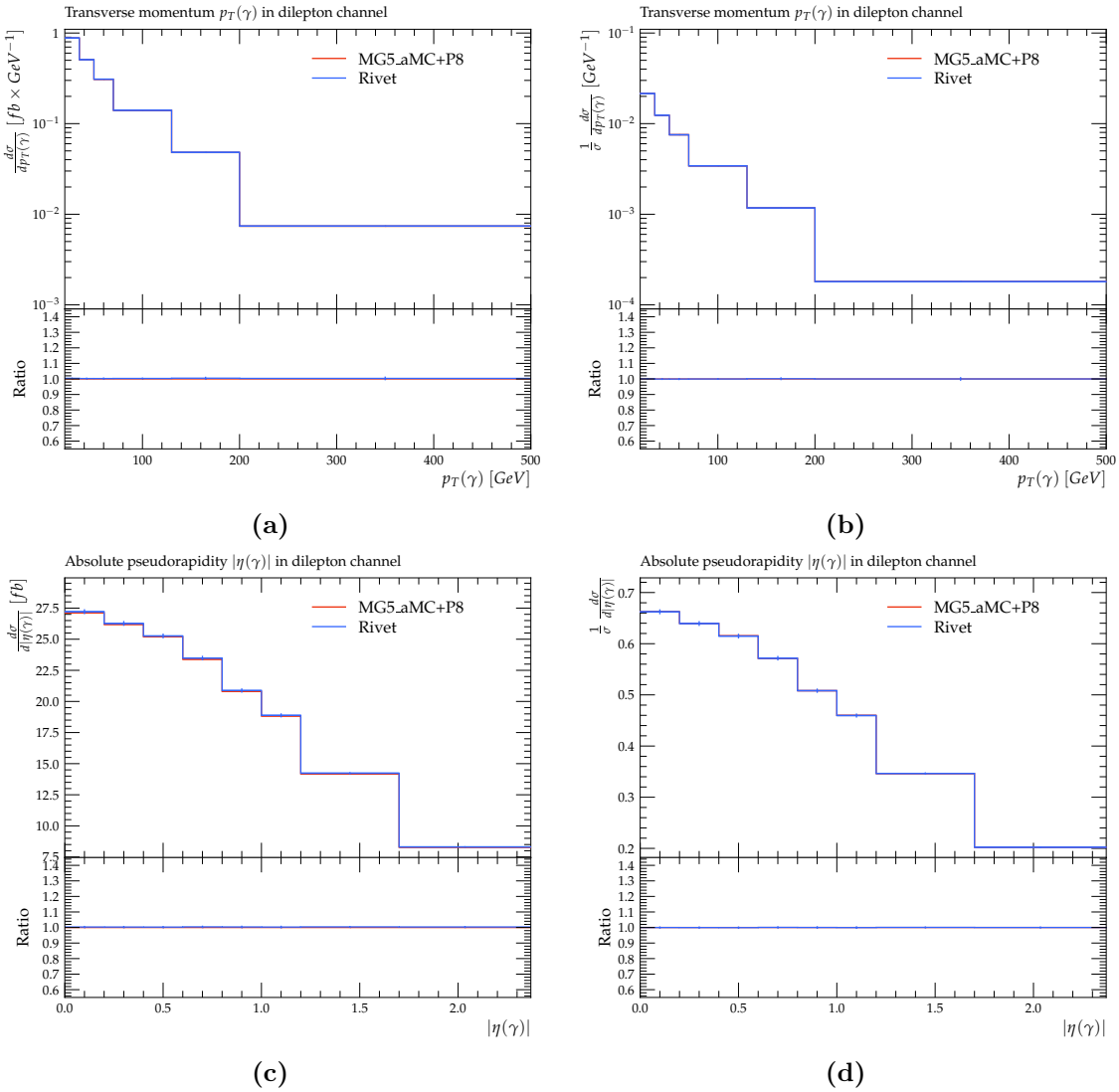

Fig. 6.11: Validation plots for $t\bar{t}\gamma$ production process. Comparison of the absolute (a,c) and normalized (b,d) cross section as a function of photon p_T (a,b) and photon $|\eta|$ (c,d) in the dilepton channel, obtained with the Rivet routine *(blue)* and the analysis code *(red)* [8].

For the purpose of completeness, the plots of the combined channels for the $t\bar{t}\gamma$ production process are shown, as these are used for theory comparisons and extrapolation to total phase space in the further analysis, see the following chapter 7.

Combined channels

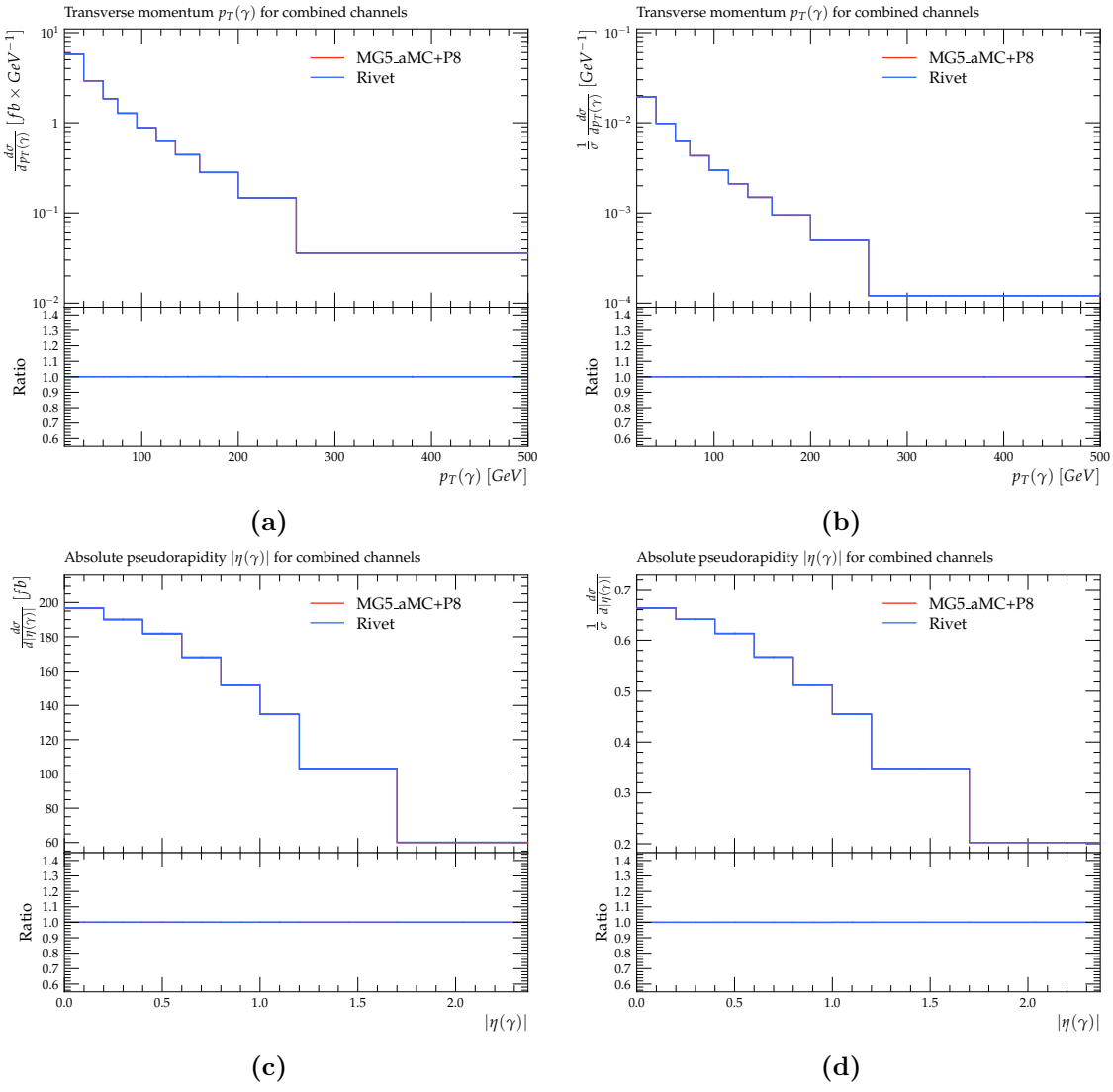

Fig. 6.12: Validation plots for $t\bar{t}\gamma$ production process. Comparison of the absolute (a,c) and normalized (b,d) cross section as a function of photon p_T (a,b) and photon $|\eta|$ (c,d) in the combined single-lepton and dilepton channels, obtained with the Rivet routine *(blue)* and the analysis code *(red)* [8].

In summary the plots show a very good agreement between the distributions obtained with MadGraph5_aMC@NLO simulation interfaced to Pythia 8 in Reference [8] and the corresponding histogram generated with the Rivet routine. So, the results are fully validated, see [7].

6.4.2 Absolute and normalised $t\bar{t}\gamma$ total differential cross section in fiducial phase space

This section continues with the results for the total $t\bar{t}\gamma$ production and decay differential cross section. The cross sections are obtained in the same phase space as the $t\bar{t}\gamma$ production process at stable particle level. In contrast to the $t\bar{t}\gamma$ production process, photons originating from the top quark decay products are regarded as signal, too.

The results of the Rivet routine are obtained from the LO $2 \rightarrow 7$ MadGraph5_aMC@NLO simulation interfaced with NNPDF2.3LO PDF set and Pythia 8 as used in [8] and described in section 4.2.

Similar to $t\bar{t}\gamma$ production, the absolute and normalised cross-sections in the single-lepton and dilepton channels are also measured for $t\bar{t}\gamma$ total as functions of photon, lepton and jet kinematic properties, and angular separations of the photon, leptons and jets. As in section 6.4.1, the distributions of $p_T(\gamma)$ and $|\eta(\gamma)|$ are shown as representative examples in single-lepton and dilepton channels. The remaining distributions of the corresponding kinematic quantities can be found in the appendix 8.

Overall there are no significant differences between the distributions obtained with MadGraph5_aMC@NLO simulation interfaced to Pythia 8 in Reference [8] and the corresponding histogram generated with the Rivet routine. Both describe the shape of the distributions well.

The comparison of $t\bar{t}\gamma$ production and $t\bar{t}\gamma$ total show that the former one has better agreement in the distributions which is according to the expectations.

Single-lepton channel

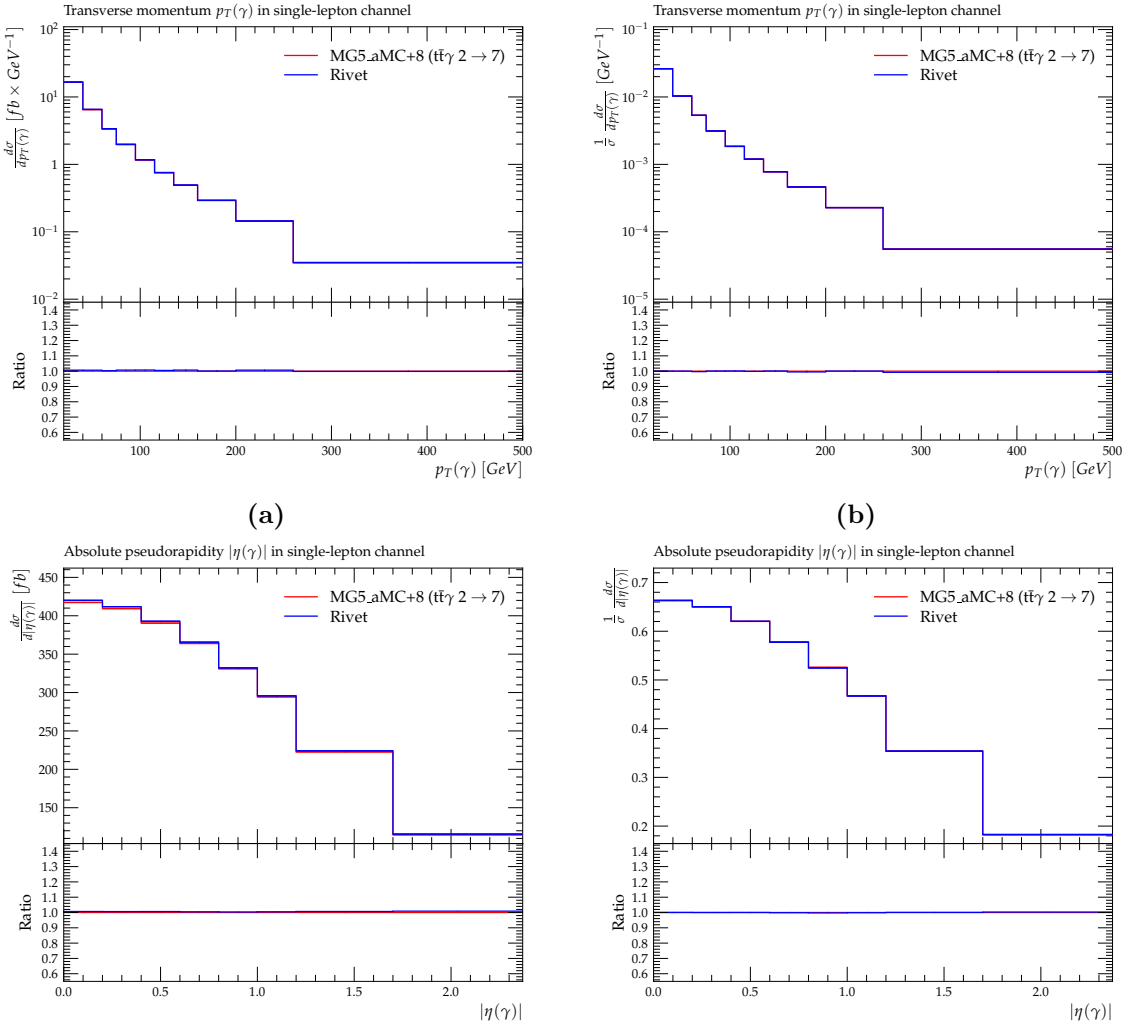

Fig. 6.13: Validation plots for total $t\bar{t}\gamma$ production and decay process. Comparison of the absolute (a,c) and normalized (b,d) differential cross section as a function of photon p_T (a,b) and photon $|\eta|$ (c,d) in the single-lepton channel, obtained with the Rivet routine *(blue)* and the analysis code *(red)* from the LO $2 \to 7$ MadGraph5_aMC@NLO simulation interfaced with Pythia 8 [8]. The last bin of the photon p_T includes overflow events.

Dilepton channel

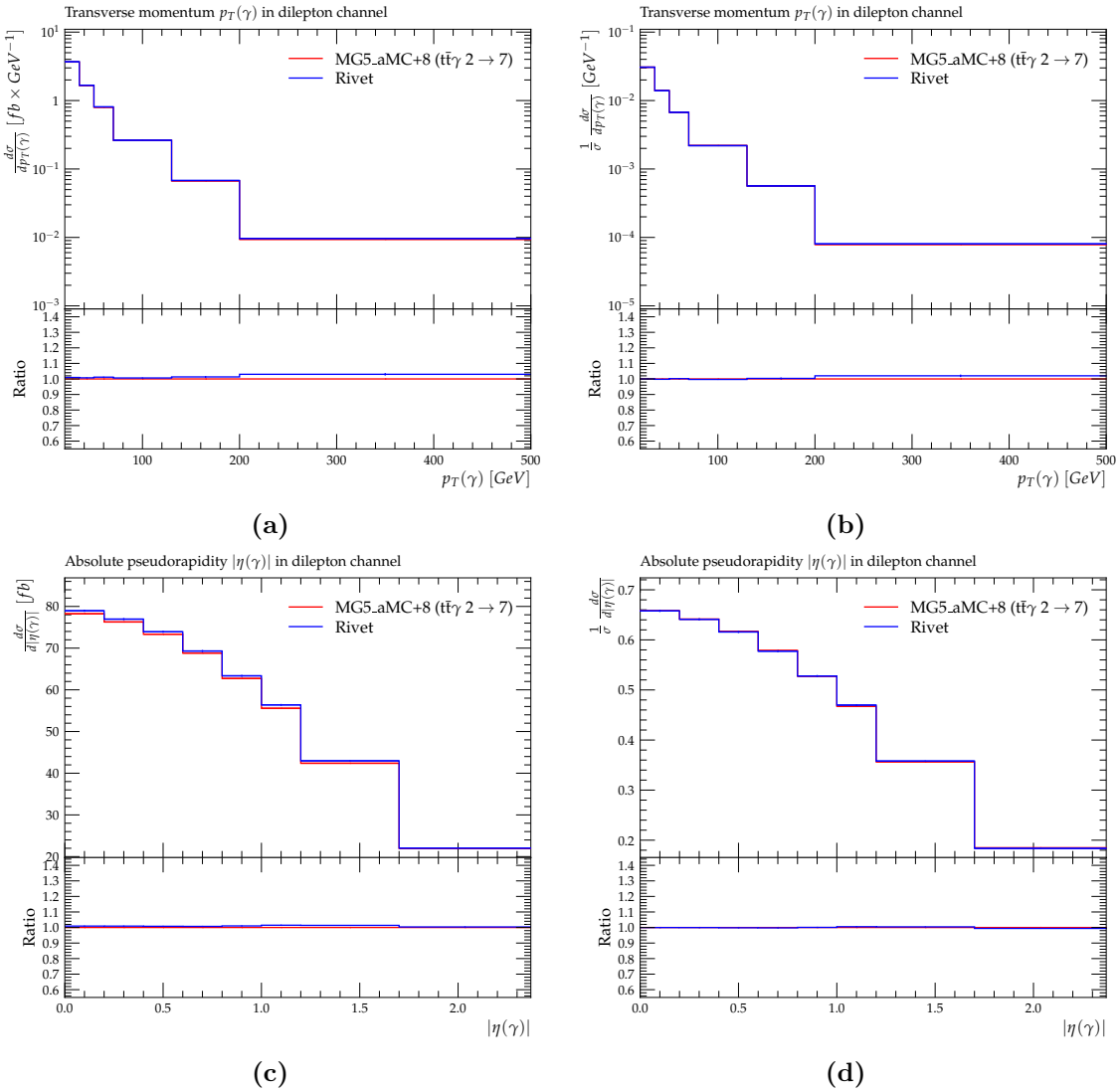

Fig. 6.14: Validation plots for total $t\bar{t}\gamma$ production and decay process. Comparison of the absolute (a,c) and normalized (b,d) differential cross section as a function of photon p_T (a,b) and photon $|\eta|$ (c,d) in the dilepton channel, obtained with the Rivet routine *(blue)* and the analysis code *(red)* from the LO $2 \to 7$ MadGraph5_aMC@NLO simulation interfaced with Pythia 8 [8]. The last bin of the photon p_T includes overflow events.

7 Analyses of top quark pair production with an additional photon

After the full validation of the Rivet routine presented in chapter 6, it can be applied for further examinations. The first part of this chapter describes the extrapolation from fiducial to total phase space at particle level for the combination of single-lepton and dilepton channels, referred to as combined channels. In a second part the results in full phase space of the $t\bar{t}$ system are compared to recent theory calculations [47].

7.1 Extrapolation from fiducial to total phase space

In Reference [47] the so-called Complete-NLO predictions for top quark pair hadroproduction in association with at least one isolated photon is computed for the first time. The set of all the possible contributions of $\mathcal{O}(\alpha_s^n \alpha^m)$ at LO and NLO is what is labelled with Complete-NLO, specified in Equation 7.1:

$$\text{NLO} = \text{LO}_1 + \text{LO}_2 + \text{LO}_3 + \text{NLO}_1 + \text{NLO}_2 + \text{NLO}_3 + \text{NLO}_4. \tag{7.1}$$

In the following the Complete-NLO is simply denoted as NLO and serves as a reference value for further comparisons.

As part of this study, an additional MC sample was generated for simulation of the total phase space. Accordingly, no requirements are placed on the $t\bar{t}$ decay products, but on the photon. Especially no requirements referred to the leptons are implemented in the MC sample. For more details see Appendix A.1.

For comparison the generated MC sample of this study contains photons passing the Frixione isolation, also used in Reference [47]. A comparison of the exact choice of parameters is given in Table 7.1.

As can be seen in Table 7.1, the parameters for the photon Frixione isolation are tighter in Reference [47], which is assumed to affect the results.

Reference	$\boldsymbol{\delta_0}$	$\boldsymbol{\epsilon_\gamma}$	**n**
Pagani et al. [47]	0.4	1	1
ATLAS [8]	0.1	0.1	2

Tab. 7.1: Comparison of the different parameters of the Frixione isolation used in References [8; 47]. The variable δ_0 is the fixed radius of isolation cone in $\eta - \phi$ space, ϵ_γ marks the maximum amount of hadronic energy (normalized to the photon energy) allowed inside the cone and n $\in \mathbb{Z}$ [32].

Therefore, photon isolation at particle level is additionally applied in the present study. Photons are required not to originate from a hadron decay and are isolated, with the condition that the sum of transverse momenta of all charged particles surrounding the photon within $\Delta R \leq 0.2$ must be smaller than 5% of its own p_T. The aim is to tighten the isolation criteria imposed by the less tight Frixione isolation used in Reference [8].

With focus on the $t\bar{t}\gamma$ case study in Reference [47], Table 7.2 presents the impact of photon isolation at particle level compared to the calculated NLO cross section in Reference [47] for different photon requirements. The results presented in Table 7.2 are obtained by using Rivet calculating the full phase space cross section of the $t\bar{t}$ system.

Requirements	$\sigma^{\text{MC total}}_{\gamma-\text{isolation}}$ **[fb]**	$\sigma^{\text{MC total}}_{\text{no }\gamma-\text{isolation}}$ **[fb]**	σ **[fb]** [47]
$p_T(\gamma) \geq 25$ GeV	$1745 \pm (2)$	$1955 \pm (2)$	1744(6)
$p_T(\gamma) \geq 50$ GeV	$947 \pm (2)$	$1041 \pm (2)$	912(5)
$p_T(\gamma) \geq 25$ GeV, $\lvert\eta(\gamma)\rvert \leq 2.5$	$1599 \pm (2)$	$1797 \pm (2)$	1557(2)
$p_T(\gamma) \geq 50$ GeV, $\lvert\eta(\gamma)\rvert \leq 2.5$	$890 \pm (2)$	$980 \pm (2)$	842(1)

Tab. 7.2: Total cross sections with different requirements on the transverse momentum $p_T(\gamma)$ and pseudorapidity $|\eta(\gamma)|$ for $t\bar{t}\gamma$ production with and without photon isolation at particle level calculated with Rivet. The uncertainties are the absolute statistical errors.

Inspecting Table 7.2, the total cross section without photon isolation is around 10% larger than for the case with included photon isolation. As expected the cross section $\sigma^{\text{MC total}}_{\text{no }\gamma-\text{isolation}}$ is larger compared to the cross section provided by Reference [47] because the isolation is looser. The isolation at particle level seems closer to the one of the calculations in Reference [47]. Finally, the comparison with the results for NLO in Table 1 of Reference [47] confirms the implementation of photon isolation into the present study since the results are similar.

This part of the thesis uses the measured differential cross sections from Reference [8] available at HEPData [44] and the same MC sample generated with MC generator MadGraph5_aMC@NLO interfaced with Pythia 8 for comparison. The differential cross sections are measured in the same fiducial region, see 6.2.2, as functions of photon kinematic variables and angular variables among others which are not in the focus for this part of the study. For this calculation consideration of the transverse momentum $p_T(\gamma)$ and the absolute pseudorapidity $|\eta(\gamma)|$ of the photon are relevant, since other variables cannot be obtained in the total phase space because they involve the decay products of the $t\bar{t}$ system.

7.1.1 Estimation of the extrapolation acceptance factor

In order to perform the extrapolation from the fiducial to the total phase space, first the extrapolation acceptance factor referred to as k in the following is calculated, which results from the ratio of the fiducial to the total cross section:

$$k = \frac{\sigma_{\text{fiducial}}}{\sigma_{\text{total}}}. \tag{7.2}$$

The additional generated MC sample with limited requirements is relevant here, as it is used for the following calculations.

The variable σ_{fiducial} is the cross section calculated at particle level in the fiducial phase space and is estimated by using the full validated Rivet routine for $t\bar{t}\gamma$ production running over the MC sample with the limited cuts.
The variable σ_{total} is the cross section in the full phase space and is calculated by using a modified version of the Rivet routine without requirements on leptons, jets and b-jets but on the photon. In order to reflect the full phase space, the Rivet routine only contains photon isolation and the photon cuts according to Reference [47], satisfying $p_T(\gamma) \geq 25$ GeV and $|\eta(\gamma)| \leq 2.5$. According to the procedure for determining σ_{fiducial}, the total cross section σ_{total} is then calculated by running the modified Rivet routine over the generated MC sample with the limited cuts.

The uncertainties considered in the extrapolation factor arise from statistical uncertainties due to the limited events in the MC simulations and systematic uncertainties related to the modelling of the physical processes. The modelling uncertainties for $t\bar{t}\gamma$ production account for effects from the choice of QCD scales and PDF sets. The effects of the QCD scale uncertainties are estimated by separately varying up and down the renormalisation scale μ_R and factorisation scale μ_F by a factor of two relative to the nominal value. As already mentioned in section 4.2 the renormalisation and factorisation scales were set to $0.5 \times \sum_i \sqrt{m_i^2 + p_{T,i}^2}$, where m_i and $p_{T,i}$ are the masses and transverse momenta of the particles generated from the matrix element (ME) calculation.
The uncertainty of the PDFs for $t\bar{t}\gamma$ production simulation is calculated by using the PDF4LHC15 prescription [48].

The following plots show the absolute differential distributions for fiducial and total phase space obtained with the MC sample at generator level related to the requirements adapted to attain the total phase space.

As shown in Figure 7.1 and Figure 7.2, the total uncertainties are dominated by the systematic uncertainties. The impact of the PDF variations has been tested and is neglected due to their minimal effect around per mill. The limited events in the MC sample lead to small statistical uncertainties varying around 1%. Due to the small size these will not be considered when computing the uncertainty of the acceptance correction.

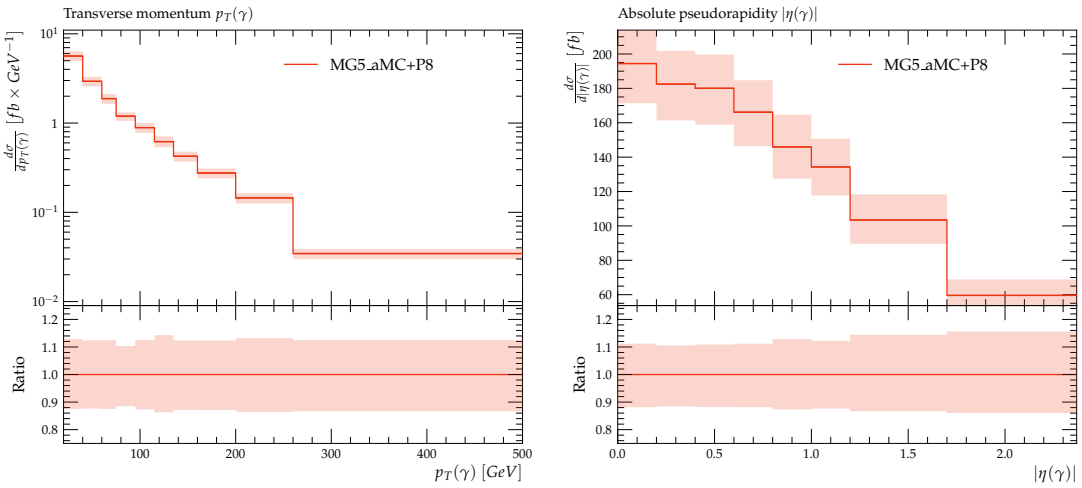

Fig. 7.1: Differential cross section distribution with nominal *(dark red)* and scale variations μ^{up} and μ^{down} *(light red)* for transverse momentum $p_T(\gamma)$ *(left)* and absolute pseudorapidity $|\eta(\gamma)|$ *(right)* of the photon in combined single-lepton and dilepton channel for fiducial phase space.

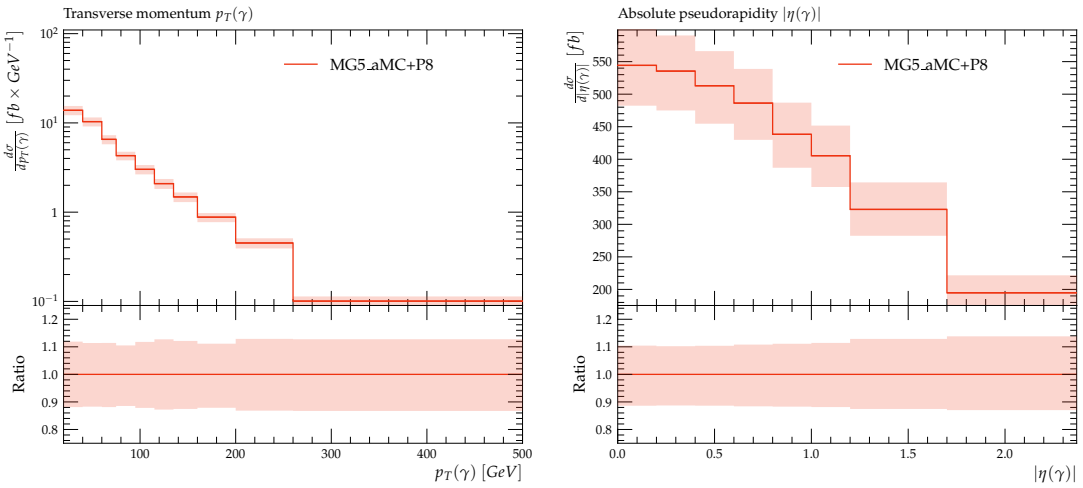

Fig. 7.2: Differential cross section distribution with nominal *(dark red)* and scale variations μ^{up} and μ^{down} *(light red)* for transverse momentum $\mathrm{p_T}(\gamma)$ *(left)* and absolute pseudorapidity $|\eta(\gamma)|$ *(right)* of the photon in combined single-lepton and dilepton channel for total phase space.

The systematic uncertainties of the acceptance factor k are estimated by varying the nominal μ_{R} and μ_{F} scales by a factor of 2.0 and 0.5 independently. The varied acceptance corrections are calculated as:

$$\mathrm{k}^{0.5}_{\mu_{\mathrm{R}}} = \frac{\sigma^{0.5\mu_{\mathrm{R}},1.0\mu_{\mathrm{F}}}_{\text{fiducial}}}{\sigma^{0.5\mu_{\mathrm{R}},1.0\mu_{\mathrm{F}}}_{\text{total}}} \qquad \text{and} \tag{7.3}$$

$$\mathrm{k}^{0.5}_{\mu_{\mathrm{F}}} = \frac{\sigma^{1.0\mu_{\mathrm{R}},0.5\mu_{\mathrm{F}}}_{\text{fiducial}}}{\sigma^{1.0\mu_{\mathrm{R}},0.5\mu_{\mathrm{F}}}_{\text{total}}}, \tag{7.4}$$

so that $\mathrm{k}^{2.0}_{\mu_{\mathrm{R}}}$ and $\mathrm{k}^{2.0}_{\mu_{\mathrm{F}}}$ can be determined equivalently.
The total uncertainty is estimated by summing both uncertainties in quadrature:

$$\Delta\mathrm{k}^{\text{up}} = \sqrt{(\mathrm{k} - \mathrm{k}^{0.5}_{\mu_{\mathrm{R}}})^2 + (\mathrm{k} - \mathrm{k}^{0.5}_{\mu_{\mathrm{F}}})^2}, \tag{7.5}$$

$$\Delta\mathrm{k}^{\text{down}} = \sqrt{(\mathrm{k} - \mathrm{k}^{2.0}_{\mu_{\mathrm{R}}})^2 + (\mathrm{k} - \mathrm{k}^{2.0}_{\mu_{\mathrm{F}}})^2}. \tag{7.6}$$

The extrapolation acceptance factor k is determined inclusively and differentially.

Inclusive

The inclusive acceptance factor k is calculated as the integral of the differential cross section distributions of $|\eta(\gamma)|$ in fiducial phase space for the combined single-lepton and dilepton channels. The inclusive acceptance factor k results in

$$\mathrm{k} = 0.3335\ ^{+0.0023}_{-0.0020}, \tag{7.7}$$

which will be used to extrapolate to the full phase space, see subsection 7.1.3. It is important to remember that the acceptance correction given in Equation 7.7 corresponds to the case of photon requirements with $\mathrm{p_T}(\gamma) \geq 25$ GeV and $|\eta(\gamma)| \leq 2.5$ and comprises the correction for the $\mathrm{t\bar{t}}$ leptonic decays only as it is later used for MC comparison. The branching ratio related to leptonic decays has to be considered when extrapolating from fiducial to total phase space of the entire $\mathrm{t\bar{t}}$ system, regardless of the decay channel of the $\mathrm{t\bar{t}}$ system.

Differential

Figure 7.3 shows the distributions of the calculated differential acceptance factor k as a function of photon $\mathrm{p_T}$ and $|\eta|$ in the combined single-lepton and dilepton channels for the same phase space requirements of $\mathrm{p_T}(\gamma) \geq 25$ GeV and $|\eta(\gamma)| \leq 2.5$ as mentioned before.

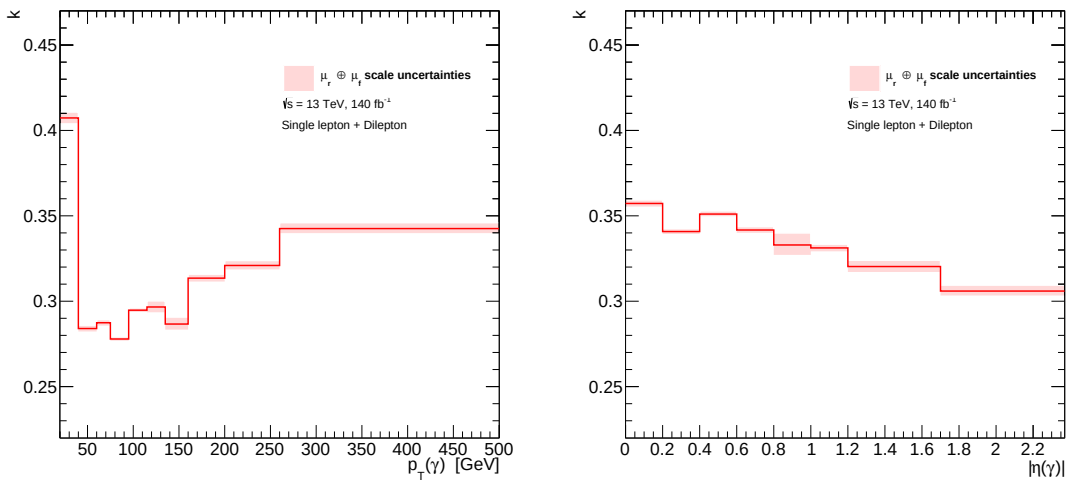

Fig. 7.3: Differential acceptance factor k of transverse momentum $\mathrm{p_T}(\gamma)$ *(left)* and absolute pseudorapidity $|\eta(\gamma)|$ *(right)* of the photon in combined single-lepton and dilepton channels.

As it can be seen in Figure 7.3 the differential form of $|\eta(\gamma)|$ shows a distribution decreasing from around 0.36 down to approximately 0.31, i.e. the acceptance factor k varies by about

5%. With regard to $p_T(\gamma)$, a deviation of 10% can even be observed. The dominant contribution is given by the first bin whose high deflection results from different MC phase space requirements for $p_T(\gamma)$. The differential k factor guarantees a correction bin by bin when extrapolating from fiducial to the total phase space of the $t\bar{t}$ system the measured cross section.

7.1.2 Extrapolation of the inclusive cross section

The acceptance k factor in Equation 7.7 has been determined for the leptonic phase space of $t\bar{t}$ decays. The inclusive cross section for $t\bar{t}\gamma$ production in combined single-lepton and dilepton channel generated by the NLO MadGraph5_aMC@NLO simulation in Reference [8] is already provided in section 5.2.

The branching ratio of BR = 54.3% [20] for leptonic decays has to be considered when extrapolating from fiducial to total phase space of the $t\bar{t}$ system. Accordingly, the extrapolation of the measured inclusive $t\bar{t}\gamma$ production cross section given in equation 5.4 yields to

$$\sigma^{\text{Data}}_{t\bar{t}\gamma_{\text{production}}} = 1762 \pm 22\ (\text{stat})\ ^{+83}_{-77}\ (\text{syst})\ ^{+25}_{-22}\ (\text{extrapolation})\ \text{fb}. \tag{7.8}$$

As already mentioned, the value is obtained for the case with $p_T(\gamma) \geq 25$ GeV and $|\eta(\gamma)| \leq 2.5$.

7.1.3 Extrapolation of the differential cross section

In the following section, the differential measured cross sections in the fiducial region provided by HEPData [44] is extrapolated. The extrapolation is done for $p_T(\gamma)$ and $|\eta(\gamma)|$ in the combined single-lepton and dilepton channels. Two cases are considered: The extrapolation to the total phase space excluding hadronic decays to show the agreement between the extrapolated fiducial data and the MadGraph5_aMC@NLO simulation interfaced to Pythia 8, simulated for this thesis. The generated sample only includes $t\bar{t}$ leptonic decays. Secondly, the extrapolation of the fiducial data to the total phase space is performed as a comparison with recent theory predictions is carried out later. Due to the exclusion of the hadronic decays in the generated MC sample the branching ratio for leptonic decays is taken into account to extrapolate to the total $t\bar{t}\gamma$ cross section. For the exact extrapolation from fiducial to total phase space, the calculation uses the differential k factor, so that a correction bin by bin is applied.

Extrapolation to the total phase space of leptonic decays of the $t\bar{t}$ system

The distributions in the combined single-lepton and dilepton channels, extrapolated considering only to $t\bar{t}\gamma$ leptonic decays, are illustrated in Figure 7.4a and Figure 7.4b, respectively.

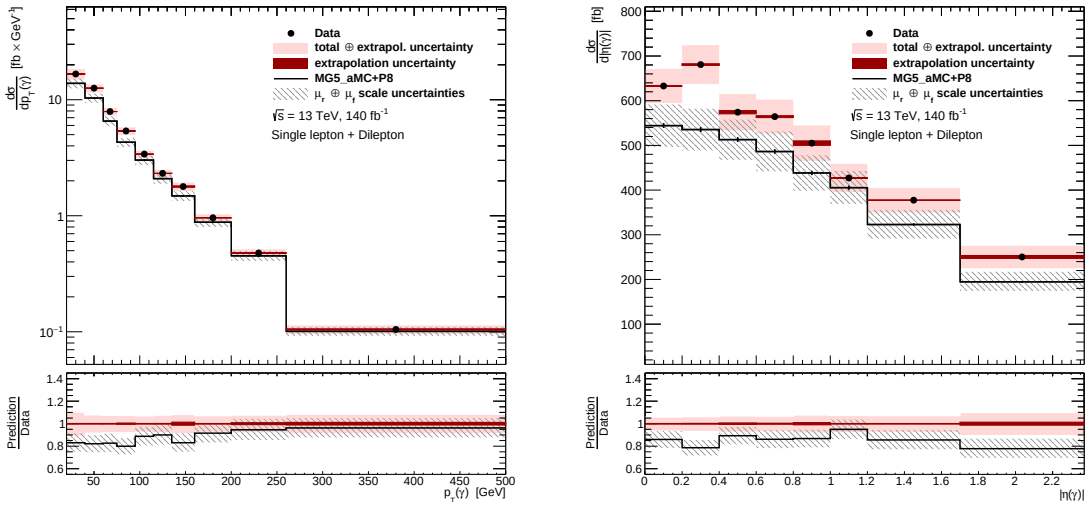

(a) **(b)**

Fig. 7.4: Absolute differential cross section as a function of photon $p_T(\gamma)$ (a) and $|\eta(\gamma)|$ (b) extrapolated to the full phase space for $t\bar{t}$ leptonic final states. Data are compared with the MadGraph5_aMC@NLO simulation interfaced to Pythia 8 simulated for this thesis. The uncertainty bands represent the combined total and extrapolation uncertainty *(pink)* or separately the extrapolation uncertainty *(red)*. The shaded area shows the uncertainty related to the renormalisation and factorisation scale. The lower panel illustrate the ratio of the prediction to the data. The last bin of the $p_T(\gamma)$ distribution includes the overflow events.

Overall, the shapes of $p_T(\gamma)$ and $|\eta(\gamma)|$ are well described. The MC predictions, normalised to the NLO cross section given by the simulation, underestimate the measured cross section. The combined total and extrapolation uncertainty of the absolute cross section in the combined channels ranges from 10% to 20% depending on the variable and the bin of the distribution. The uncertainty related to the normalisation and factorisation scale varies around 1%. Due to the limited events in the MC simulations the uncertainties for the MadGraph5_aMC@NLO simulation interfaced to Pythia 8 simulated for this thesis are higher varying around 15%.

Extrapolation to the total phase space of the $t\bar{t}$ system

The measured absolute differential cross section distributions extrapolated to the total phase space of the $t\bar{t}$ system are illustrated in Figures 7.5a and 7.5b.

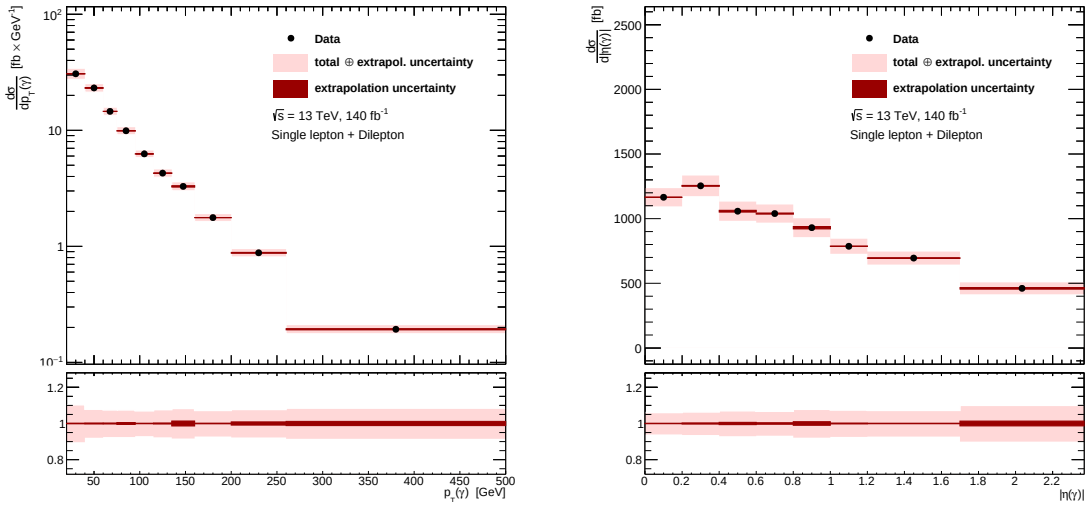

(a) **(b)**

Fig. 7.5: Absolute differential cross section as a function of photon $p_T(\gamma)$ (a) and $|\eta(\gamma)|$ (b) extrapolated to the total phase space of the $t\bar{t}$ system. The uncertainty bands represent the combined total and extrapolation uncertainty *(pink)* or separately the extrapolation uncertainty *(red)*. The last bin of the $p_T(\gamma)$ distribution includes the overflow events.

Requirements	$\sigma^{\text{extrapolation}}_{\text{Data}}$ **[fb]**
$p_T(\gamma) \geq 25$ GeV	$1913 \pm 24\ (\text{stat})\ ^{+90}_{-84}\ (\text{syst})\ ^{+27}_{-24}\ (\text{extrapolation})$
$p_T(\gamma) \geq 50$ GeV	$1038 \pm 13\ (\text{stat})\ ^{+49}_{-46}\ (\text{syst})\ ^{+15}_{-13}\ (\text{extrapolation})$
$p_T(\gamma) \geq 25$ GeV, $\lvert\eta(\gamma)\rvert \leq 2.5$	$1762 \pm 22\ (\text{stat})\ ^{+83}_{-77}\ (\text{syst})\ ^{+25}_{-22}\ (\text{extrapolation})$
$p_T(\gamma) \geq 50$ GeV, $\lvert\eta(\gamma)\rvert \leq 2.5$	$976 \pm 12\ (\text{stat})\ ^{+46}_{-43}\ (\text{syst})\ ^{+14}_{-12}\ (\text{extrapolation})$

Tab. 7.3: Results for the extrapolated data. Calculated total cross sections for different requirements with γ – isolation at particle level on the transverse momentum $p_T(\gamma)$ and pseudorapidity $|\eta(\gamma)|$ for $t\bar{t}\gamma$ production.

7.2 Comparison to theoretical calculations at NLO

With focus on the $t\bar{t}\gamma$ case study in Reference [47], a comparison between the theoretical calculations at NLO and the analysis results for the extrapolated measured cross section is drawn for the different photon requirements. Table 7.4 shows a summary of the results for the extrapolated data in various phase spaces comparisons to the complete calculations in Reference [47] for $t\bar{t}\gamma$ production, and already gives a hint of possible deviations related to the final comparison between the measured cross section extrapolation and the recent theory predictions.

Requirements with $\gamma -$ isolation	$\sigma_{\text{Data}}^{\text{extrapolation}}$ **[fb]**	σ **[fb]** [47]
$p_T(\gamma) \geq 25$ GeV	1913 $\pm$ 24	1744 $\pm$ 6
$p_T(\gamma) \geq 50$ GeV	1038 $\pm$ 13	912 $\pm$ 5
$p_T(\gamma) \geq 25$ GeV, $\lvert\eta(\gamma)\rvert \leq 2.5$	1762 $\pm$ 22	1557 $\pm$ 2
$p_T(\gamma) \geq 50$ GeV, $\lvert\eta(\gamma)\rvert \leq 2.5$	976 $\pm$ 12	842 $\pm$ 1

Tab. 7.4: Results for the extrapolated data in various phase spaces comparisons to the complete calculations in Reference [47] for $t\bar{t}\gamma$ production. The uncertainties are the absolute statistical errors.

As the definition of the isolation is slightly different for the Frixione photon isolation tighter in Reference [47], no exact matching is expected. Although the Frixione photon isolation has been made more stringent by including photon isolation at the particle level, it can be seen from Table 7.4 that there is a constant deviation of about 10% relative to the values provided by Reference [47]. The relative error of the statistical uncertainty related to the extrapolation is about 1%.

The differential cross section distributions are compared side by side in Figure 7.6. However, given the different binning and ranges the differential distributions are in good agreement. The extrapolated data slightly overestimates the prediction given by Reference [47] which

corresponds to the expectations. Since the inclusive cross section is affected by a constant deviation of data, the differential cross section is also affected.

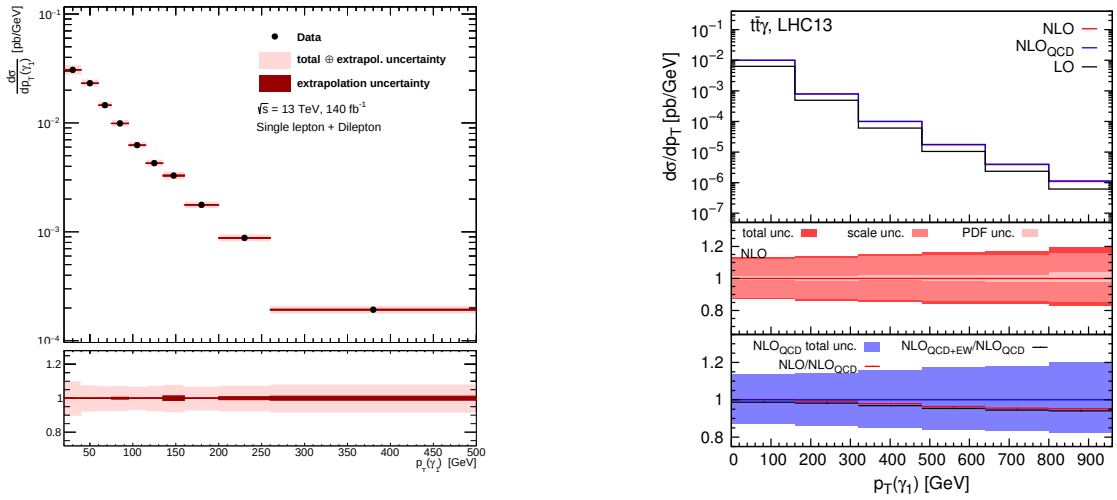

(a) **(b)**

Fig. 7.6: Extrapolated differential cross section distribution of transverse momentum p_T of the isolated photon for the case with $p_T \geq 25$ GeV and $|\eta(\gamma)| \leq 2.5$ (a), compared to theoretical predictions [47] (b) for $t\bar{t}\gamma$ production.

8 Conclusion

The aim of this master's thesis was the development of a Rivet routine for the $t\bar{t}\gamma$ production process as well as the total $t\bar{t}\gamma$ production and decay process according to Reference [8]. The code mimics the definitions of the fiducial phase space at stable particle level focussing on single-lepton and dilepton $t\bar{t}$ decay channels and the combined ones. The validation of the Rivet routine is performed with MC simulations at NLO ($t\bar{t}\gamma$ production) and LO ($t\bar{t}\gamma$ total). The Rivet routine is full validated and available at [7]. As a key aspect this allows to compare simulations and future calculations with the measurement in a convenient way.

Furthermore, the measured $t\bar{t}\gamma$ production cross section obtained by Reference [8] and provided by [44] is extrapolated from fiducial to total phase space of the $t\bar{t}$ system. The results for the extrapolated measured data for various phase spaces obtained in this analysis are:

$p_T(\gamma) \geq 25$ GeV $\quad \sigma_{t\bar{t}\gamma_{\text{production}}} = 1913 \pm 24\ (\text{stat})\ ^{+90}_{-84}\ (\text{syst})\ ^{+27}_{-24}\ (\text{extrapolation})$ fb

$p_T(\gamma) \geq 50$ GeV $\quad \sigma_{t\bar{t}\gamma_{\text{production}}} = 1038 \pm 13\ (\text{stat})\ ^{+49}_{-46}\ (\text{syst})\ ^{+15}_{-13}\ (\text{extrapolation})$ fb

$p_T(\gamma) \geq 25$ GeV, $|\eta(\gamma)| \leq 2.5$ $\quad \sigma_{t\bar{t}\gamma_{\text{production}}} = 1762 \pm 22\ (\text{stat})\ ^{+83}_{-77}\ (\text{syst})\ ^{+84}_{-84}\ (\text{extrapolation})$ fb

$p_T(\gamma) \geq 50$ GeV, $|\eta(\gamma)| \leq 2.5$ $\quad \sigma_{t\bar{t}\gamma_{\text{production}}} = 976 \pm 12\ (\text{stat})\ ^{+46}_{-43}\ (\text{syst})\ ^{+14}_{-12}\ (\text{extrapolation})$ fb

The measured data overestimates the corresponding theory predictions, which is according to the expectations. The relative deviation between measurement and theory is a constant around 10%.

The $t\bar{t}\gamma$ process will be further analysed for the ATLAS publications in 2025. The measurement and the analysis of this process is crucial for testing the interactions of top quarks and photons, for testing top quark properties and possibly detect BSM deviations. There is a great need to calculate precise SM predictions for this class of process, so it is necessary to improve existing frameworks by developing new implementations.

Appendix

A Code

```
import MadGraphControl.MadGraphUtils
MadGraphControl.MadGraphUtils.MADGRAPH_PDFSETTING={
    'central_pdf':260000,
    'pdf_variations':[260000,90900],
    'alternative_pdfs':None,
    'scale_variations':[0.5,1,2],}

from MadGraphControl.MadGraphUtils import *
# General settings
nevents=int(2*1.1*runArgs.maxEvents)

process = """
import model loop_sm-no_b_mass
define p = g u c d s b u~ c~ d~ s~ b~
generate p p > t t~ a QED=1 QCD=2 [QCD]
output -f"""

dec = """
define w+child = e+ mu+ ta+ ve vm vt u c d~ s~
define w-child = e- mu- ta- ve~ vm~ vt~ u~ c~ d s
decay t > w+ b, w+ > w+child w+child
decay t~ > w- b~, w- > w-child w-child
"""

settings = {'lhe_version'   :'3.0',
    'maxjetflavor'  :5,
    'parton_shower' :'PYTHIA8',
    'ptl'           :0.,
    'ptgmin'        :15.,
    'R0gamma'       :0.1,
    'xn'            :2,
    'epsgamma'      :0.1,
    'ptj'           :0.,
    'etal'          :-1.0,
    'etagamma'      :5.0,
    'mll_sf'        :0.,
    'dynamical_scale_choice':'3',
    'nevents'       :nevents}

```

List. A.1: Extract of the MadGraph configuration file showing the settings for the generated MC sample, without requirements for the $t\bar{t}$ decay products, but for the photon.

B Additional figures for the validation of the Rivet routine

Kinematic distributions for $t\bar{t}\gamma$ production

Single-lepton channel

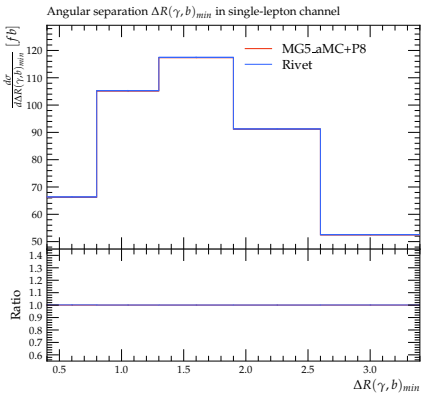

(a)

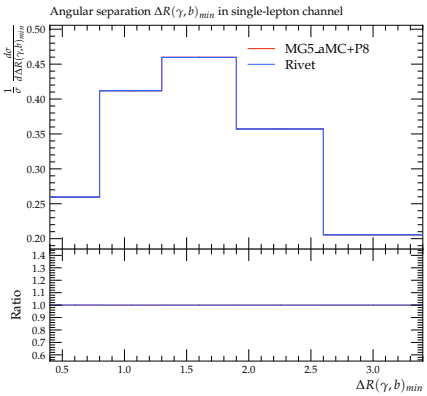

(b)

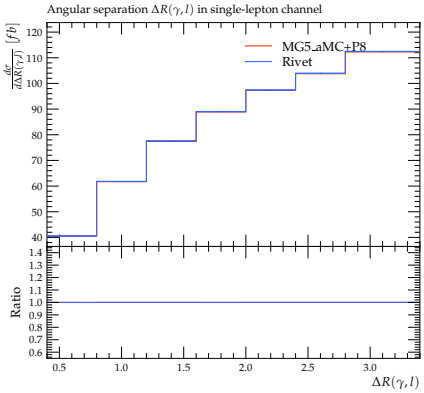

(c)

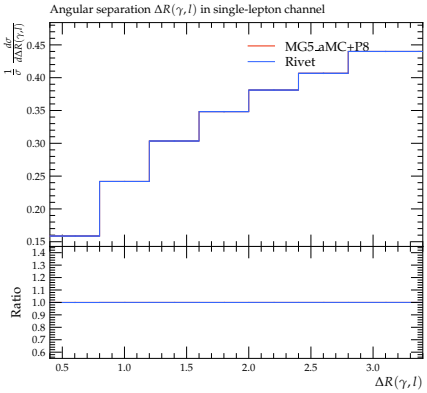

(d)

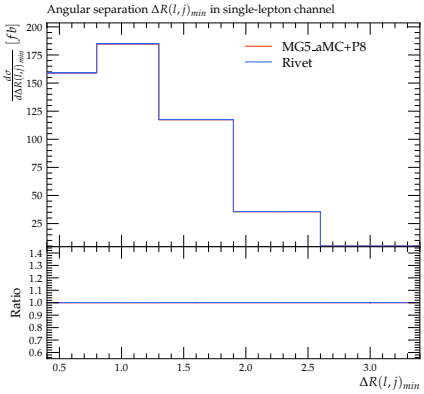

(e)

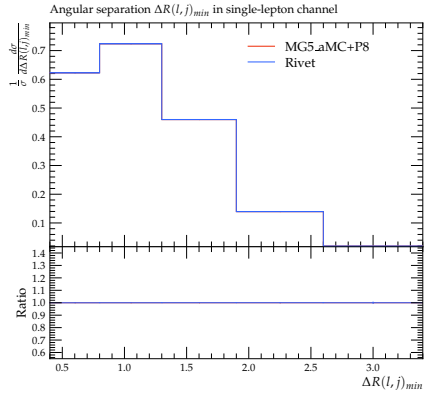

(f)

Fig. B.1: Validation plots for $t\bar{t}\gamma$ production process.

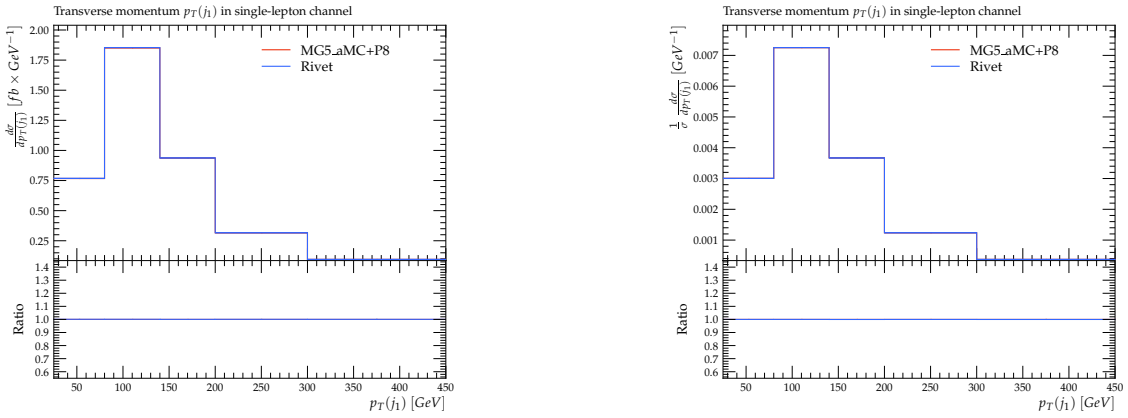

(a) **(b)**

Fig. B.2: Validation plots for $t\bar{t}\gamma$ production process.

Dilepton channel

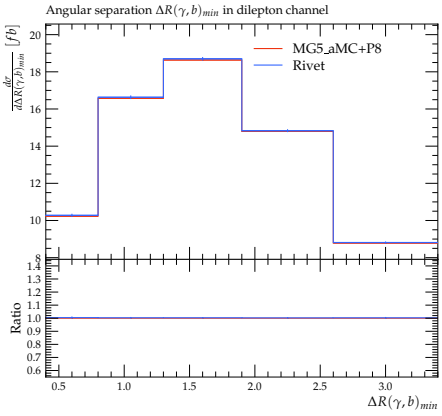

(a)

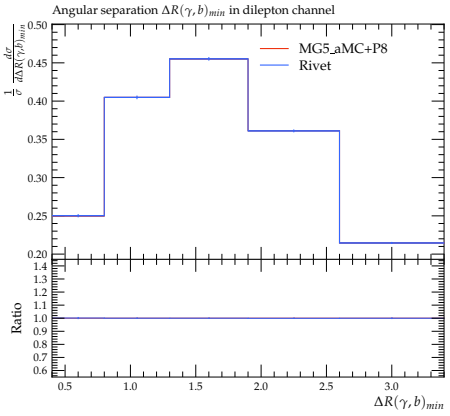

(b)

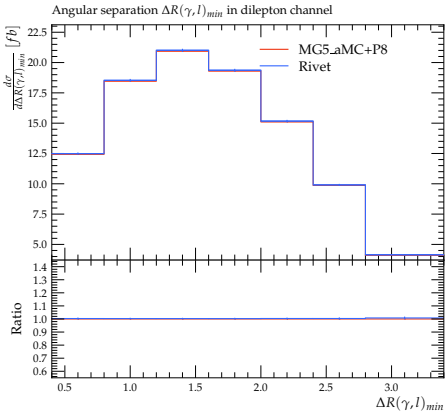

(c)

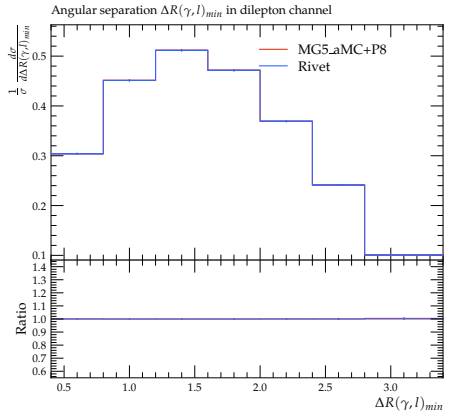

(d)

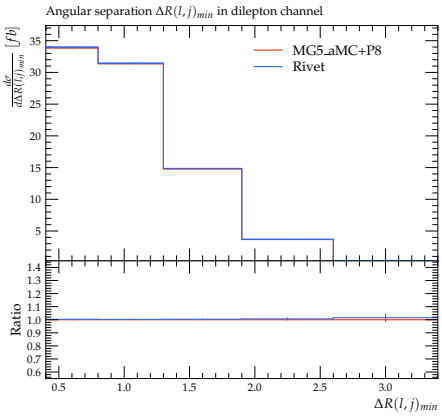

(e)

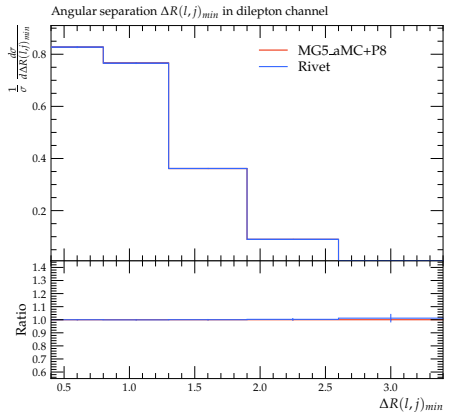

(f)

Fig. B.3: Validation plots for $t\bar{t}\gamma$ production process.

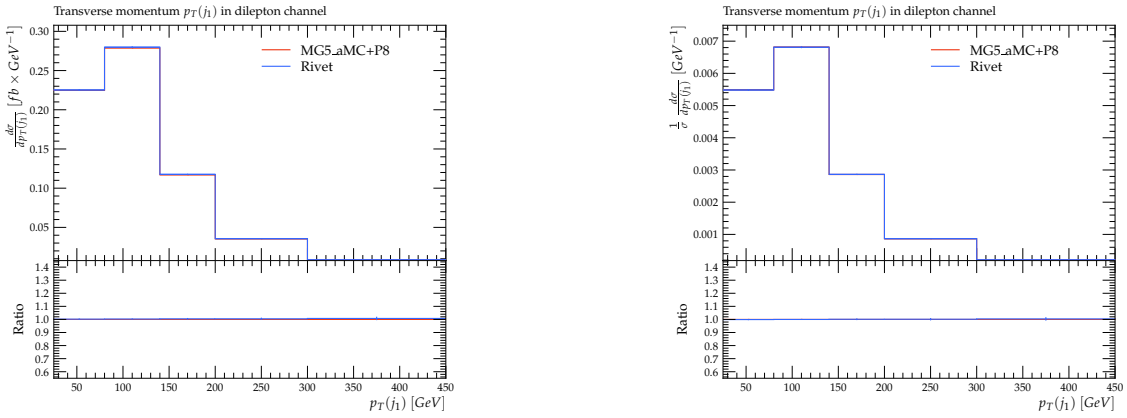

(a) **(b)**

Fig. B.4: Validation plots for $t\bar{t}\gamma$ production process.

Kinematic distributions for $t\bar{t}\gamma$ total

Single-lepton channel

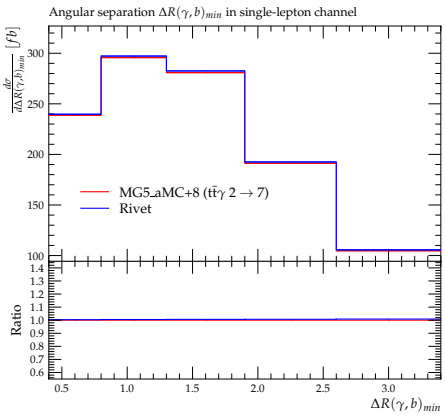

(a)

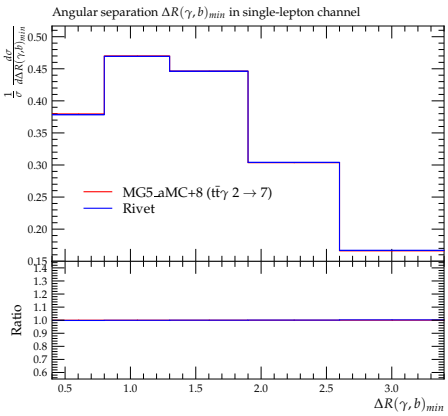

(b)

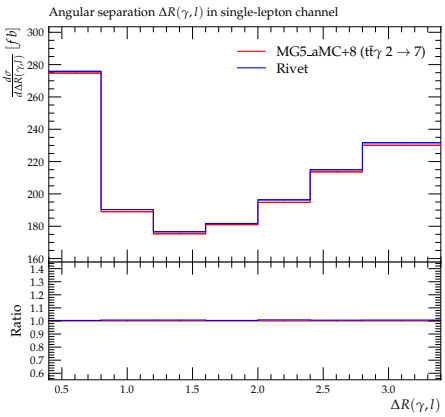

(c)

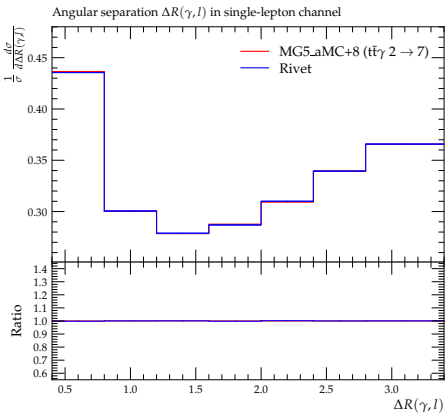

(d)

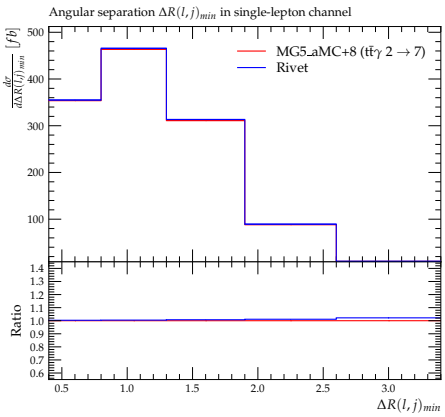

(e)

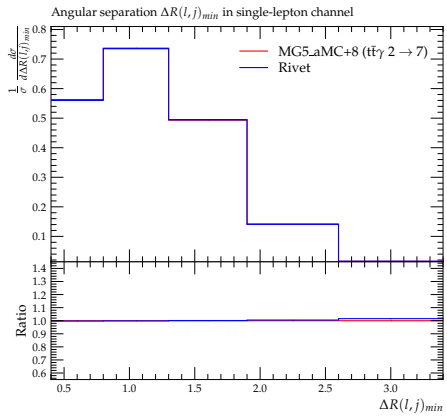

(f)

Fig. B.5: Validation plots for $t\bar{t}\gamma$ total process.

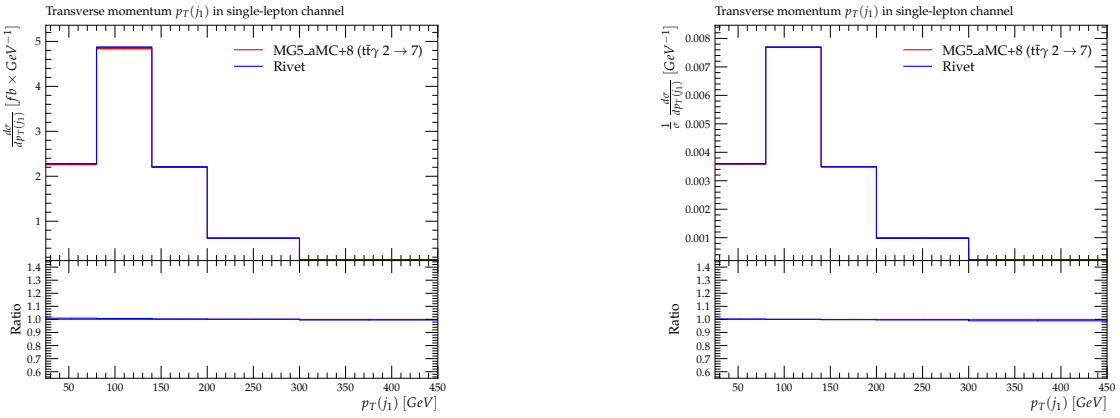

(a) **(b)**

Fig. B.6: Validation plots for $t\bar{t}\gamma$ total process.

Dilepton channel

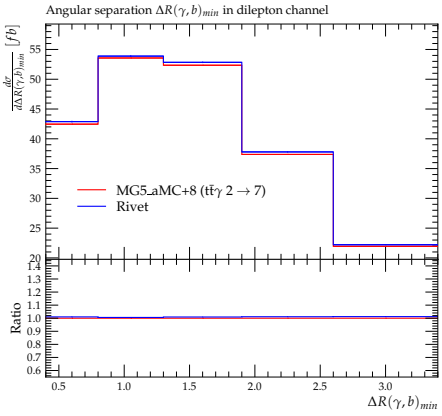

(a)

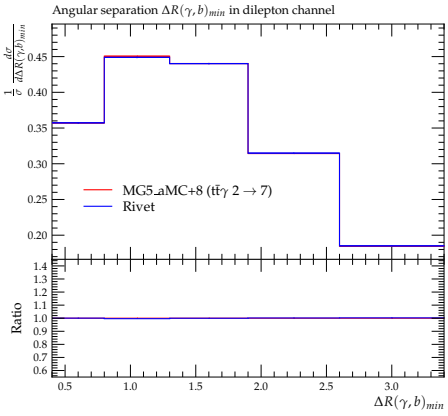

(b)

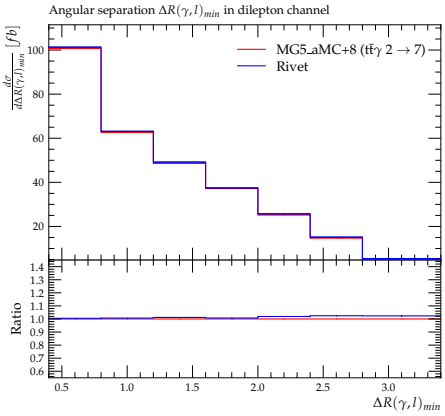

(c)

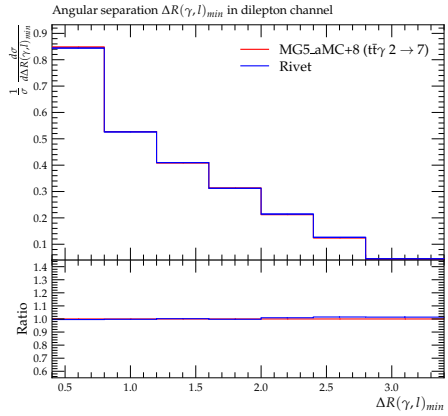

(d)

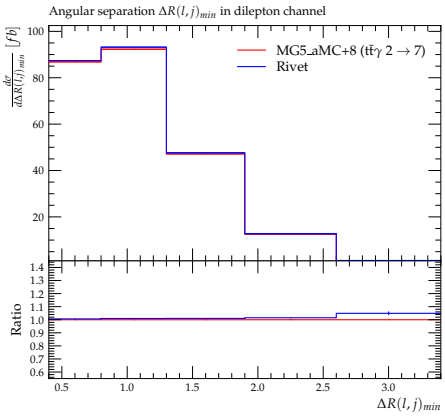

(e)

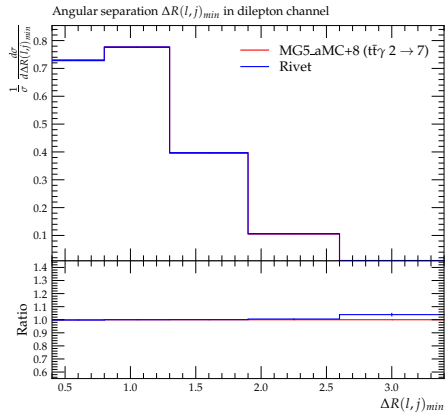

(f)

Fig. B.7: Validation plots for $t\bar{t}\gamma$ total process.

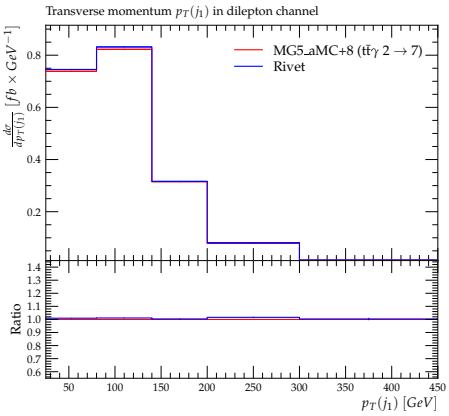

(a)

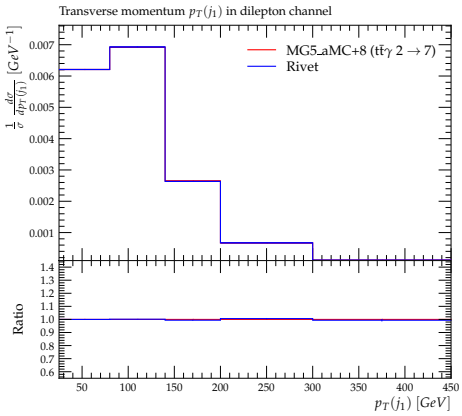

(b)

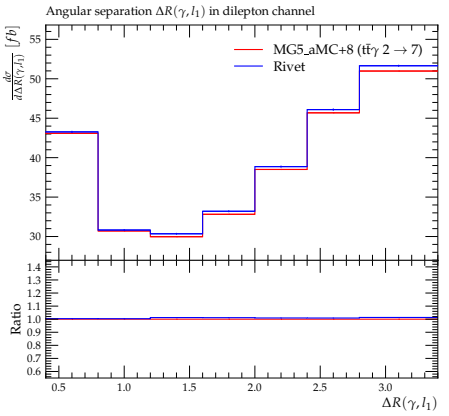

(c)

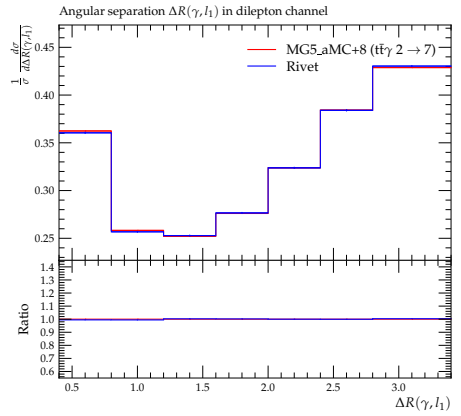

(d)

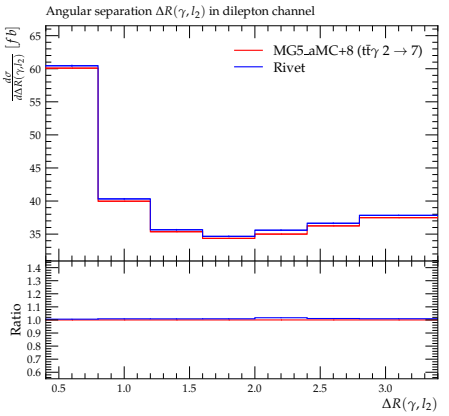

(e)

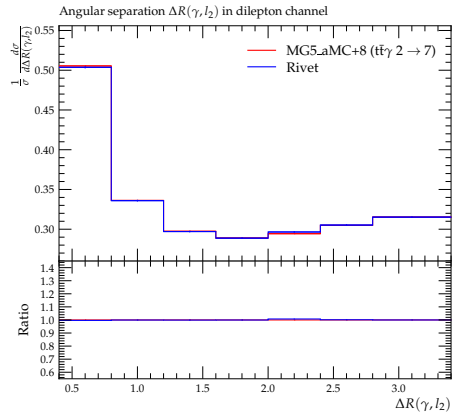

(f)

Fig. B.8: Validation plots for $t\bar{t}\gamma$ total process.

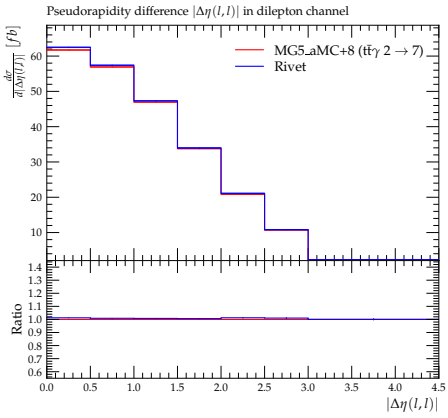

(a)

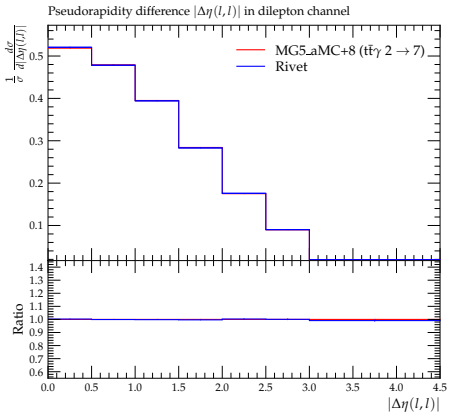

(b)

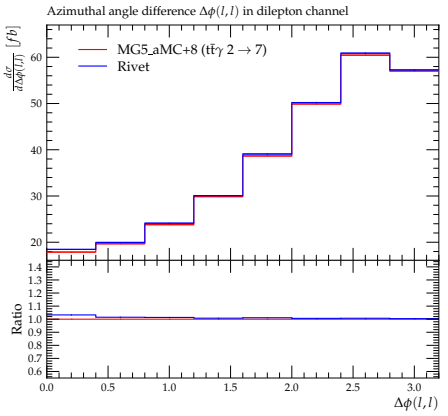

(c)

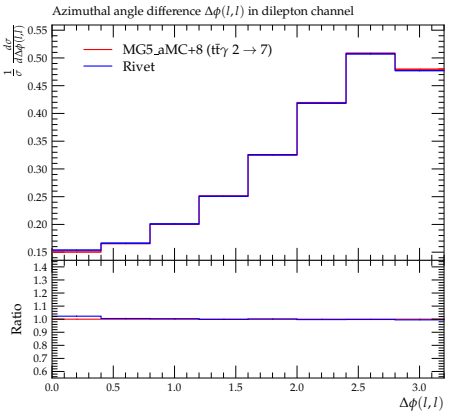

(d)

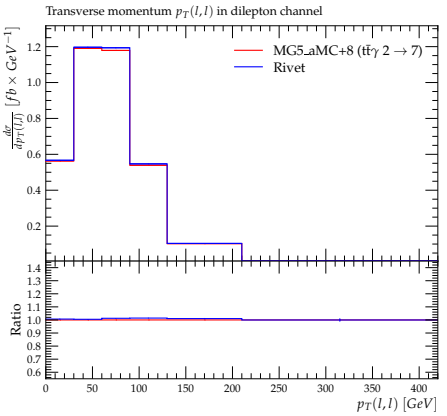

(e)

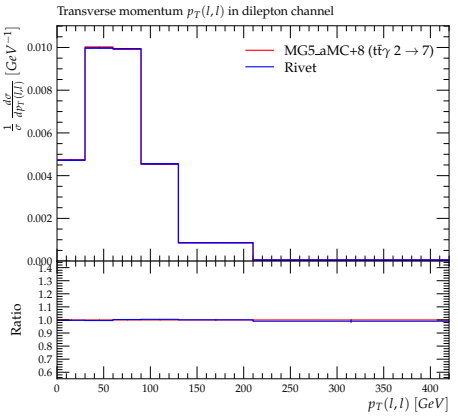

(f)

Fig. B.9: Validation plots for $t\bar{t}\gamma$ total process.

Bibliography

[1] G. Aad et al., *Observation of a new particle in the search for the Standard Model Higgs boson with the ATLAS detector at the LHC*, Physics Letters B **716** (2012), p. 1, DOI: 10.1016/j.physletb.2012.08.020.

[2] G. T. J. Arnison et al., *Experimental observation of isolated large transverse energy electrons with associated missing energy at* $\sqrt{s} = 540GeV$, Phys. Lett. B **122** (1983), p. 103, DOI: 10.5170/CERN-1983-004.123.

[3] M. Banner et al., *Observation of single isolated electrons of high transverse momentum in events with missing transverse energy at the CERN* $\bar{p}p$ *collider*, Phys. Lett. B **122** (1983), p. 476, DOI: 10.1016/0370-2693(83)91605-2.

[4] G. T. J. Arnison et al., *Experimental observation of lepton pairs of invariant mass around* $95GeV/c^2$ *at the CERN SPS collider*, Phys. Lett. B **126** (1983), p. 398, DOI: 10.1016/0370-2693(83)90188-0.

[5] P. Bagnaia et al., *Evidence for* $Z0 \to e^+e^-$ *at the CERN* $\bar{p}p$ *collider*, Phys. Lett. B **129** (1983), p. 130, DOI: 10.1016/0370-2693(83)90744-X.

[6] G. Charpak et al., *The use of multiwire proportional counters to select and localize charged particles*, Nuclear Instruments and Methods **62** (1968), p. 262, DOI: https://doi.org/10.1016/0029-554X(68)90371-6.

[7] S. Mueller and C. Diez Pardos, *Rivet analyses reference ATLAS 2024 I2768921*, 2024, URL: https://rivet.hepforge.org/analyses/ATLAS_2024_I2768921.

[8] The ATLAS Collaboration, *Measurements of inclusive and differential cross-sections of* $t\bar{t}\gamma$ *production in pp collisions at* $\sqrt{s}$ *= 13 TeV with the ATLAS detector*, Journal of High Energy Physics (2024), DOI: 10.1007/jhep10(2024)191.

[9] S. Chatrchyan et al., *Observation of a new boson at a mass of 125 GeV with the CMS experiment at the LHC*, Physics Letters B **716** (2012), p. 30, DOI: 10.1016/j.physletb.2012.08.021.

[10] M. Gonzalez-Garcia and M. Maltoni, *Phenomenology with massive neutrinos*, Physics Reports **460** (2008), p. 1, DOI: 10.1016/j.physrep.2007.12.004.

[11] S. Navas et al., *Review of Particle Physics*, Phys. Rev. D **110** (3 2024), p. 030001, DOI: 10.1103/PhysRevD.110.030001.

[12] M. Marcolli, *Mathematicians look at particle physics*, 2008, URL: https://www.math.fsu.edu/~marcolli/PopTalkSlidesFinal.pdf.

[13] LHC Top Physics Working Group, *LHCTopWG Summary Plots*, 2024, URL: https://twiki.cern.ch/twiki/bin/view/LHCPhysics/LHCTopWGSummaryPlots.

[14] The ATLAS and CDF and CMS and D0 Collaborations, *First combination of Tevatron and LHC measurements of the top-quark mass*, 2014, arXiv: 1403.4427 [hep-ex].

[15] F. Abe et al., *Observation of Top Quark Production in $\bar{p}p$ Collisions with the Collider Detector at Fermilab*, Physical Review Letters **74** (1995), p. 2626, DOI: 10.1103/physrevlett.74.2626.

[16] S. Abachi et al., *Observation of the Top Quark*, Physical Review Letters **74** (1995), p. 2632, DOI: 10.1103/physrevlett.74.2632.

[17] V. M. Abazov et al., *Observation of Single Top-Quark Production*, Phys. Rev. Lett. **103** (9 2009), p. 092001, DOI: 10.1103/PhysRevLett.103.092001.

[18] T. Aaltonen et al., *Observation of Electroweak Single Top-Quark Production*, Phys. Rev. Lett. **103** (9 2009), p. 092002, DOI: 10.1103/PhysRevLett.103.092002.

[19] Particle Data Group et al., *Review of Particle Physics*, Progress of Theoretical and Experimental Physics (2020), p. 083C01, DOI: 10.1093/ptep/ptaa104.

[20] P. D. Group et al., *Review of Particle Physics*, Progress of Theoretical and Experimental Physics (2020), p.741, DOI: 10.1093/ptep/ptaa104.

[21] The CDF Collaboration, T. Aaltonen, *Evidence for $t\bar{t}\gamma$ production and measurement of $\frac{\sigma_{t\bar{t}\gamma}}{\sigma_{t\bar{t}}}$*, Physical Review D **84** (2011), DOI: 10.1103/physrevd.84.031104.

[22] The ATLAS Collaboration, *Observation of top-quark pair production in association with a photon and measurement of the $t\bar{t}\gamma$ production cross section in pp collisions at $\sqrt{s} = 7$ TeV using the ATLAS detector*, Physical Review D **91** (2015), DOI: 10.1103/physrevd.91.072007.

[23] M. Worek, *Modelling of top quark decays in $t\bar{t}\gamma$ production at the LHC*, 2021, arXiv: 2101.07712 [hep-ph].

[24] R. D. Ball et al., *Parton distributions for the LHC run II*, Journal of High Energy Physics (2015), DOI: 10.1007/jhep04(2015)040.

[25] E. Mobs, *The CERN accelerator complex - August 2018. Complexe des accélérateurs du CERN - Août 2018* (2018), General Photo, URL: https://cds.cern.ch/record/2636343.

[26] The ATLAS Collaboration, *The ATLAS Experiment at the CERN Large Hadron Collider*, Journal of Instrumentation **3** (2008), S08003, DOI: 10.1088/1748-0221/3/08/S08003.

[27] J. Pequenao and P. Schaffner, *How ATLAS detects particles: diagram of particle paths in the detector*, 2013, URL: https://cds.cern.ch/record/1505342.

[28] J. Alwall et al., *The automated computation of tree-level and next-to-leading order differential cross sections, and their matching to parton shower simulations*, Journal of High Energy Physics (2014), DOI: 10.1007/jhep07(2014)079.

[29] R. Frederix et al., *The automation of next-to-leading order electroweak calculations*, Journal of High Energy Physics (2018), DOI: 10.1007/jhep07(2018)185.

[30] C. Bierlich et al., *A comprehensive guide to the physics and usage of PYTHIA 8.3*, SciPost Phys. Codebases (2022), p. 8, DOI: 10.21468/SciPostPhysCodeb.8.

[31] R. D. Ball et al., *Parton distributions for the LHC run II*, Journal of High Energy Physics (2015), DOI: 10.1007/jhep04(2015)040.

[32] S. Frixione, *Isolated photons in perturbative QCD*, Physics Letters B **Volume 429, Issues 3–4** (1998), Pages 369, URL: https://www.sciencedirect.com/science/article/pii/S0370269398004547.

[33] D. J. Lange, *The EvtGen particle decay simulation package*, Nuclear Instruments and Methods in Physics Research Section A: Accelerators, Spectrometers, Detectors and Associated Equipment **462,1-2** (2001), p. 152, URL: https://doi.org/10.1016/S0168-9002(01)00089-4,https://www.sciencedirect.com/science/article/pii/S0168900201000894.

[34] S. Frixione et al., *Angular correlations of lepton pairs from vector boson and top quark decays in Monte Carlo simulations*, Journal of High Energy Physics (2007), p. 081, DOI: 10.1088/1126-6708/2007/04/081.

[35] P. Artoisenet et al., *Automatic spin-entangled decays of heavy resonances in Monte Carlo simulations*, Journal of High Energy Physics (2013), DOI: 10.1007/jhep03(2013)015.

[36] The ATLAS Collaboration, *Measurement of the charge asymmetry in top-quark pair production in association with a photon with the ATLAS experiment*, Physics Letters B **843** (2023), p. 137848, DOI: 10.1016/j.physletb.2023.137848.

[37] The ATLAS Collaboration, *Measurements of inclusive and differential fiducial cross-sections of $t\bar{t}\gamma$ production in leptonic final states at $\sqrt{s} = 13$ TeV in ATLAS*, The European Physical Journal C **79** (2019), DOI: 10.1140/epjc/s10052-019-6849-6.

[38] The ATLAS Collaboration, *Measurements of inclusive and differential fiducial cross-sections of $t\bar{t}\gamma$ production in leptonic final states at $\sqrt{s} = 13$ TeV in ATLAS*, The European Physical Journal C **79** (2019), DOI: 10.1140/epjc/s10052-019-6849-6.

[39] The CMS Collaboration, *Measurement of the inclusive and differential $t\bar{t}\gamma$ cross sections in the single-lepton channel and EFT interpretation at $\sqrt{s} = 13$ TeV*, Journal of High Energy Physics (2021), DOI: 10.1007/jhep12(2021)180.

[40] The CMS Collaboration, *Measurement of the inclusive and differential $t\bar{t}\gamma$ cross sections in the dilepton channel and effective field theory interpretation in proton-proton collisions at $\sqrt{s} = 13$ TeV*, Journal of High Energy Physics (2022), DOI: 10.1007/jhep05(2022)091.

[41] G. Bevilacqua et al., *Off-shell vs on-shell modelling of top quarks in photon associated production*, Journal of High Energy Physics (2020), DOI: 10.1007/jhep03(2020)154.

[42] A. Tumasyan et al., *Measurement of the inclusive and differential $t\bar{t}\gamma$ cross sections in the dilepton channel and effective field theory interpretation in proton-proton collisions at $\sqrt{s} = 13$ TeV*, Journal of High Energy Physics (2022), DOI: 10.1007/jhep05(2022)091.

[43] G. Aad et al., *Measurements of inclusive and differential cross-sections of combined $t\bar{t}\gamma$ and $tW\gamma$ production in the $e\mu$ channel at 13 TeV with the ATLAS detector*, Journal of High Energy Physics (2020), DOI: 10.1007/jhep09(2020)049.

[44] The ATLAS Collaboration, *Measurements of inclusive and differential cross-sections of $t\bar{t}\gamma$ production in pp collisions at $\sqrt{s} = 13$ TeV with the ATLAS detector*, HEPData (collection), 2024, URL: https://doi.org/10.17182/hepdata.146899.

[45] M. Cacciari, G. P. Salam and G. Soyez, *The catchment area of jets*, Journal of High Energy Physics (2008), p. 005, DOI: 10.1088/1126-6708/2008/04/005.

[46] HEPForge, *Rivet:FastJets Class Reference*, 2025, URL: https://rivet.hepforge.org/code/dev/classRivet_1_1FastJets.html.

[47] D. Pagani et al., *Automated EW corrections with isolated photons: $t\bar{t}\gamma$, $t\bar{t}\gamma\gamma$ and $t\gamma j$ as case studies*, Journal of High Energy Physics (2021), DOI: 10.1007/jhep09(2021)155.

[48] J. Butterworth et al., *PDF4LHC recommendations for LHC Run II*, Journal of Physics G: Nuclear and Particle Physics **43** (2016), p. 023001, DOI: 10.1088/0954-3899/43/2/023001.